Title:

Pseudoirreversible inhibition elicits persistent efficacy of a sphigosine-1-phosphate receptor-1 antagonist

Authors:

Yuya Maruyama[1, 2, 3], Yusuke Ohsawa[3], Takayuki Suzuki[3], Yuko Yamauchi[3], Kohsuke Ohno[3], Hitoshi Inoue[3], Akitoshi Yamamoto[3], Morimichi Hayashi[3], Yuji Okuhara[3], Wataru Muramatsu[1, 2], Kano Namiki[1, 2], Maki Miyauchi[1, 2], Takahisa Miyao[1], Naho Hagiwara[1], Tatsuya Ishikawa[1, 2], Kenta Horie[1], Mio Hayama[1], Nobuko Akiyama[1,2], Takatsugu Hirokawa[4,5] and Taishin Akiyama[1, 2, *]

Affiliations:

[1]Laboratory for Immune Homeostasis, RIKEN Center for Integrative Medical Sciences, Yokohama 230-0045, Japan

[2]Immunobiology, Graduate School of Medical Life Science, Yokohama City University, Yokohama 230-0045, Japan

[3]Central Research Laboratory, Kissei Pharmaceutical Co., Ltd., 4365-1 Hotaka-Kashiwabara, Azumino, Nagano 399-8304, Japan

[4]Division of Biomedical Science, Faculty of Medicine, University of Tsukuba, 1-1-1 Tennodai, Tsukuba, Ibaraki 305-8575, Japan

[5]Transborder Medical Research Center, University of Tsukuba, 1-1-1 Tennodai, Tsukuba, Ibaraki 305-8575, Japan

Contact Information: Taishin Akiyama, Ph.D.

Postal address: 1-7-22 Suehiro-cho, Tsurumi-ku, Yokohama 230-0045, Japan

Email: taishin.akiyama@riken.jp

Abstract

Sphingosine 1-phosphate receptor 1 (S1PR1), a G protein-coupled receptor, is required for lymphocyte trafficking, and is a promising therapeutic target in inflammatory diseases. To find potent S1PR1 antagonists, identification of the structural basis for drug efficacy is important. Here, we synthesized a novel antagonist, KSI-6666, that persistently inhibits S1PR1 activity and effectively suppresses pathogenic inflammation. Metadynamics simulation suggested that the interaction of a benzene ring moiety in KSI-6666 with a methionine residue in the ligand-binding pocket of S1PR1 inhibits the dissociation of KSI-6666 from S1PR1, generating a metastable binding state. Consistently, *in vitro* functional and mutational analyses revealed that KSI-6666 causes pseudoirreversible inhibition of S1PR1, dependent on the methionine residue of the protein and substituents on the distal benzene ring of KSI-6666. Moreover, *in vivo* study suggested that this pseudoirreversible inhibition is responsible for the persistent activity of KSI-6666. These findings will contribute to the rational design of potent S1PR1 antagonists for the treatment of inflammatory disorders.

Introduction

Sphingosine 1-phosphate (S1P), which is a metabolite of membrane sphingolipids, regulates cell migration, inflammatory response, angiogenesis and neurogenesis[1]. Physiological functions of S1P are mediated by its binding to five subtypes of the sphingosine 1-phosphate receptor, which belongs to the G protein-coupled receptor (GPCR) family[1]. Among S1P receptors, S1P receptor 1 (S1PR1) is critical for lymphocyte trafficking and progression of immune and inflammatory responses. Binding of S1P to S1PR1 causes activation of Gi, a subfamily of guanine nucleotide-binding proteins, leading to the inhibition of adenylate cyclase-induced cAMP synthesis and subsequent activation of several intracellular signaling pathways. The binding also induces the phosphorylation-dependent recruitment of β-arrestin and subsequent cellular internalization of the ligand–receptor complex.

Given its roles in lymphocyte trafficking, S1PR1 is a target for the treatment of autoimmune and inflammatory diseases. FTY720, also named fingolimod, is a first-generation S1PR1 modulator that was approved as a drug for treatment of multiple sclerosis (MS)[2,3]. Mechanistically, FTY720 is phosphorylated *in vivo* into FTY720-phosphate (FTY720-P), which serves as a functional antagonist of S1P receptors including S1PR1.[2] Thus, binding of FTY720-P activates S1PR1 signaling, leading to the internalization and subsequent degradation of S1PR1. As a result, administration of FTY720 causes long-lasting inhibition of S1PR1 signaling through the depletion of cell surface S1PR1. However, in addition to lymphocyte trafficking, S1PR1 controls the function of cardiac cells[4]. Therefore, agonistic activity of FTY720 provokes bradycardia[4-6], a temporal reduction of the heart rate, as an undesirable side-effect.

Competitive antagonists of S1PR1 would not cause side effects ascribed to the agonistic activity. W146, which has a similar structure to FTY720-P, was the first competitive antagonist of S1PR1[7,8]. However, the *in vivo* efficacy of W146 is poor and transient[8]. In addition to FTY720-based S1PR1 modulators such as W146, structurally distinct S1PR1 modulators have been developed[9]. Among them, NIBR-0213 is a competitive antagonist of S1PR1 that displayed persistent efficacy *in vivo*[10]. Further development of potent S1PR1 antagonists may offer more effective methods of treatment for autoimmune diseases such as MS.

The efficacy of a drug is affected by its residence time in the target protein in addition to its equilibrium binding affinity and pharmacokinetics[11-13]. Therefore, the determination of drug–protein binding kinetics is useful for predicting drug efficacy[14]. Some studies have shown that antagonists with slow dissociation rates cause pseudoirreversible inhibition of targets with insurmountable antagonism[15-17], which is defined as the inability of the pre-bound antagonist to be completely replaced by a competing ligand in nonequilibrium conditions[18]. Drugs with pseudoirreversible inhibition properties show persistent *in vivo* efficacies because of their long residence time[19].

Computational approaches can be used to investigate the binding behavior of drugs to target proteins[20-26]. Molecular dynamics simulations can be used to evaluate binding and release pathways, kinetics, and thermodynamics[27]. Metadynamics (MetaD), which is a sampling method enhanced by escaping local free energy minima[24,28], and other approaches[24] are available for detailed description of binding and unbinding kinetics[20,22,23,25]. In addition to these force field-based calculations, quantum mechanical methods such as the fragment molecular orbital (FMO) method have been applied for *ab initio* characterization of drug interactions with proteins[29,30]. However, the linking of these computational estimations for binding and dissociation kinetics to practical *in vitro* and *in vivo* efficacies of a drug remains a challenge.

In this study, we aimed to find a potent S1PR1 antagonist with persistent efficacy and to elucidate the structural basis underlying its persistency. We discovered a S1PR1 antagonist, KSI-6666, that showed potent and persistent efficacy *in vivo*. A combination of MetaD simulation, FMO calculation, and experimental verification suggests that KSI-6666 is a pseudoirreversible inhibitor because of its hindered dissociation from S1PR1. The pseudoirreversible inhibition requires the interaction between a methionine residue in S1PR1 and an aromatic ring moiety of KSI-6666.

Results

KSI-6666 is a potent and selective antagonist of S1PR1 and suppresses intestinal inflammation

We started developing new competitive antagonists of S1PR1 from the lead compound **1** (Fig. 1a), which is similar to a compound previously discovered by Novartis company. For the optimization of compound **1**, we performed *in vitro* screening to evaluate the antagonistic effects of compounds on GTP binding to Gi in S1PR1-expressing human embryonic kidney (HEK293) cells induced by an S1PR1 agonist made by Merck (Merck S1PR1 agonist)[31] (Fig. 1a). In addition, the reduction in blood leukocyte count induced by inhibition of S1PR1 after the oral administration of compounds was evaluated in *in vivo* screening in rats (Fig. 1b). The selection identified a novel S1PR1 antagonist *(RS)*-KSI-6666 (hereafter referred to as KSI-6666 for simplicity), a racemic form with a half-maximal inhibitory concentration (IC_{50}) of 6.4 nM in GTP binding assay. Reduction in blood leukocyte count caused by KSI-6666 was observed at 48 h after administration (Fig 1b), and thus it may be more persistent than NIBR-0213 since its response duration was reported as 24 h at 30 mg/kg administration[10]. Consequently, we concluded that KSI-6666 is a potent antagonist with persistent efficacy.

We further confirmed that KSI-6666 had no agonistic activity on S1PR1 signaling. Binding of an agonist to S1PR1 results in the activation of Gi and receptor internalization[1]. Consistently, FTY720-P and the Merck S1PR1 agonist led to an increment in the GTP binding to Gi and a decrease of surface S1PR1 on HEK293 cells (Fig. 1c and d). In contrast, treatment with KSI-6666 caused a decrease in the GTP binding activity and an increment in the surface amount of S1PR1 even in the absence of agonists (Fig. 1c and d). These data indicated that KSI-6666 has no agonistic activity and indeed has inverse agonistic activity, which is defined as inhibition of spontaneous receptor activation[32], thereby suppressing the constitutive activation of S1PR1. In the case of W146, inverse agonistic activity was detected at only high concentrations (Fig. 1d).

We next tested the antagonistic activity of KSI-6666 toward ligand binding to S1PR1 in other assays. S1PR1 activation increases Ca^{2+} mobilization in cells over-expressing Gα15, a subunit

of G protein alpha. KSI-6666 competitively inhibited the agonist-dependent Ca^{2+} mobilization of S1PR1, but not for other S1PRs (Fig. 1e and Extended Data Fig. 1). KSI-6666 inhibited mouse and rat S1PR1 with similar inhibitory activity as human S1PR1, demonstrating its cross-species efficacy (Fig. 1e and Extended Data Fig. 1). Furthermore, the agonist-dependent internalization of S1PR1 on HEK293 cells was antagonized by KSI-6666 in a dose-dependent manner (Fig. 1f). *In vivo*, in guinea pig, pretreatment with KSI-6666 completely blocked the reduction of heart rate induced by administration of FTY720 (Fig. 1g). These data suggest that KSI-6666 is a selective and competitive antagonist of S1PR1 in mammals, and therefore would not cause bradycardia as a side effect.

S1PR1 signaling is critical for lymphocyte trafficking, and therefore the inhibition of S1PR1 impairs lymphocyte migration from lymphoid organs to the bloodstream, thereby causing lymphopenia[1]. In Transwell assays *in vitro*, the addition of KSI-6666 inhibited the motility of murine splenocytes induced by S1P (Fig. 1h). Consistently, flow cytometric analysis showed that the numbers of CD4-, CD8-, and CD19-positive cells in mouse blood were significantly reduced 4 h after intravenous injection of KSI-6666 (Fig. 1i). In contrast, injection of W146 caused a slight reduction of B cell number in the blood at 1 h, but not at 4 h (Fig. 1i). In addition to rodents, the administration of KSI-6666 effectively diminished blood lymphocyte numbers in cynomolgus monkeys, confirming efficacy in primates. The data suggest that, compared with W146, KSI-6666 has a potent and persistent effect in suppressing lymphocyte trafficking in rodents and primates.

In addition to the lymphocyte trafficking, S1PR1 modulators have a common effect on the endothelial barrier[7]. Consistently, we observed that the repetitive oral administration of KSI-6666 caused vascular hyperpermeability-related effects such as edema in the lungs (Extended Data Fig. 2 and Supplementary Table 1), further supporting that KSI-6666 can inhibit the functions of S1PR1 *in vivo*.

We further considered whether KSI-6666 suppresses inflammation in pathological rodent models. Studies in a T-cell transfer colitis model (Fig. 2a) and an oxazolone-induced colitis model (Fig. 2b) revealed that administration of KSI-6666 significantly suppressed the induced

intestinal inflammation, comparable with the effect of KRP-203, a functional agonistic inhibitor of S1PR1[33]. These data suggest that KSI-6666 is a potent and persistent S1PR1 antagonist with anti-inflammatory activity.

Molecular dynamics simulation reveals a slow dissociation of KSI-6666 from S1PR1

The structure of KSI-6666 is largely divisible into a zwitterionic part consisting of a carboxylic acid and an aliphatic tertiary amine, and a hydrophobic moiety consisting of two aromatic rings with bulky substituents; one chiral carbon atom in the linker is also between the two aromatic rings (marked with an asterisk in Fig. 1a). Among the enantiomers, the S1PR1 inhibitory activity of the *(R)*- KSI-6666 was more potent than that of the *(S)*- KSI-6666 (Fig 3a and b). This suggests that the spatial arrangement of the distal benzene ring may be important for the potent binding and inhibitory activity toward S1PR1.

To gain more insight into the structural basis of the activity of KSI-6666, we first performed molecular docking analysis for the binding of *(R)*-KSI-6666 with S1PR1. Co-crystallographic data for the complex of W146 and S1PR1 (PDB: 3v2y)[34] were used for the docking study of *(R)*-KSI-6666. The pose of *(R)*-KSI-6666 with the lowest binding free energy was selected from among the docking complexes, and compared with the crystallographic structure of W146 (Fig. 3c). Overlay of the pose of *(R)*-KSI-6666 with the W146 structure suggested that the two compounds would adopt a similar pose in the ligand-binding pocket. Thus, a polar group (a carboxylic acid in *(R)*-KSI-6666 and a phosphate in W146) and a benzene ring (the internal benzene ring of *(R)*-KSI-6666 and the benzene ring of W146) overlapped, and the end of the hydrophobic moiety (CF_3– in *(R)*-KSI-6666 and CH_3– in W146) was in a similar position for the two inhibitors. The minimum binding free energy to S1PR1 was estimated to be −11.79 kcal/mol for *(R)*-KSI-6666 and −8.83 kcal/mol for W146, supporting stable binding of *(R)*-KSI-6666.

To detail the interaction between *(R)*-KSI-6666 and S1PR1, the FMO method was performed for the docking complexes, and the interfragment interaction energies (IFIEs) were estimated. Thus, S1PR1 (amino acids 15–314) was fragmented into units containing a single amino acid, and the

interaction energies between each unit and *(R)*-KSI-6666 were evaluated by molecular orbital calculations. Moreover, pair interaction energy decomposition analysis (PIEDA) in FMO calculation divides the IFIE into four energy components: electrostatic (ES), exchange repulsion (EX), charge-transfer and mixing term (CT+mix), and dispersion (DI) energies that in part contribute to hydrophobic interactions. The FMO method suggested strong ES interactions of the zwitterionic moiety of *(R)*-KSI-6666 with residues Arg120, Tyr29, Glu121, and Lys34 of S1PR1 (Fig. 3d). Residues Phe125, Asn101, Leu297, Trp269, Phe210, Leu272, Phe273, and Tyr98 contribute to the interaction with *(R)*-KSI-6666 through DI energy (Fig. 3d). Thus, FMO calculation supported that hydrophobic interaction due to DI energy, along with ES energy, is critical for the binding of *(R)*-KSI-6666 to S1PR1.

The dissociation kinetics of an antagonist from a target molecule are one of the critical determinants for its therapeutic effect[11-13]. Because KSI-6666 showed persistent efficacy compared with W146, we next performed MetaD simulation, which is used for biasing toward dissociation by applying external forces, to explore and compare the dissociation process from S1PR1 between *(R)*-KSI-6666 and W146. In total, 10 simulation runs for 100 ns each were performed for each compound. A plot of binding free energy profiles (kcal/mol) against the distance of *(R)*-KSI-6666 (or W146) from the binding site in enhanced sampling using MetaD simulation suggested that a stable binding state of *(R)*-KSI-6666, but not of W146, may exist around 2 □ away from the docking position (Fig. 3e). Moreover, to evaluate the dissociation process, the root-mean-square distance (RMSD) of *(R)*-KSI-6666 and W146 from the docking position was plotted against the simulation time. Assuming that the ligand was dissociated from S1PR1 when the RMSD was >30 □, dissociation of W146 occurred in 7 of 10 runs by 100 ns from the start of the simulation (Fig. 3f), but dissociation of *(R)*-KSI-6666 occurred in only 4 of 10 runs. Furthermore, in four runs for *(R)*-KSI-6666, the RMSD converged at around 2 □ after 100 ns, which is consistent with the binding free energy profiles (Fig. 3e). Overall, MetaD simulation suggested that *(R)*-KSI-6666 is more resistant than W146 to dissociation from S1PR1.

To verify the findings from MetaD simulation, binding and dissociation properties of KSI-6666 were determined experimentally by the functional reversibility assay[35] (Fig. 3g). After S1PR1-

expressing cells were pretreated with KSI-6666 at various concentrations, serially diluted amounts of the agonistic FTY720-P were added (Fig. 3g). The replacement of KSI-6666 with agonist FTY720-P on S1PR1 was monitored via the level of cellular surface S1PR1 (Fig. 3g). As described above, in the absence of the agonist, the addition of KSI-6666 caused inverse agonistic activity (labeled "w/o" in Fig. 3g). As expected, the addition of FTY720-P or S1P ligand caused the replacement of KSI-6666 in a dose-dependent manner. Of note, however, the maximum agonist effect (E_{max}) did not reach 100% when the pretreatment was with a high concentration of KSI-6666 (Fig. 3g). Furthermore, E_{max} decreased with increasing concentrations of pretreated KSI-6666 (Fig. 3g right). This phenomenon occurred for both agonists, FTY720-P and the natural ligand S1P. Moreover, the increment of GTP binding activity on agonist addition did not reach the maximum in the presence of a high concentration of KSI-6666 (Fig. 3g). This indicates that the replacement of KSI-6666 by the agonists was not complete in the assay. In contrast, when W146 was used in the pretreatment, the agonistic responses reached the maximum level, suggesting the complete replacement of W146 by these agonists. Consequently, these data suggest that KSI-6666 is an insurmountable antagonist with pseudoirreversible inhibitory activity, which is consistent with the hindered dissociation of KSI-6666 predicted by MetaD simulation.

Residue Met124 of S1PR1 is critical for the pseudoirreversible inhibition by KSI-6666

We next sought to determine the interaction responsible for the pseudoirreversible inhibition of S1PR1 by KSI-6666. When the MetaD trajectories of *(R)*-KSI-6666 were visually inspected, *(R)*-KSI-6666 appeared to intimately interact with hydrophobic residue Met124 of S1PR1, whereas W146 did not (Fig. 4a and Supplementary Videos 1 and 2). To confirm this observation, 100 snapshots from each MetaD trajectory were selected at equal intervals and analyzed by using the protein–ligand interaction fingerprint (PLIF) tool implemented in Molecular Operating Environment (MOE) software, in which the interaction between a compound and each amino acid residue in a protein is represented as a fingerprint bit according to its interaction type. The frequency of bit entry for *(R)*-KSI-6666 relative to W146 was estimated. Data suggested that, among the amino acids that *(R)*-KSI-6666 contacts during the dissociation process, Met124 was the amino acid with the largest difference in contact frequency between

(R)-KSI-6666 and W146, with *(R)*-KSI-6666 making more frequent surface contact with Met124 than doing W146 (Fig. 4b). The PLIF analysis also showed that arene interaction and hydrogen bonding of the side chain, but neither ionic nor other types of hydrogen bonding, contribute to the interaction of *(R)*-KSI-6666 with Met124, suggesting a major involvement of hydrophobic interaction in the contact of *(R)*-KSI-6666 with Met124. Overall, the MetaD simulation suggested that the slow dissociation of *(R)*-KSI-6666 from S1PR1 depends on its contact with Met124, which may result in the pseudoirreversible inhibition of this inhibitor.

We experimentally verified the significance of Met124 for the interaction predicted by the MetaD analysis. HEK293 cells expressing mutant S1PR1 where Met124 was replaced by Val (Val124) or Leu (Leu124) were established (Extended Data Fig. 3). Functional reversibility assays by measuring the internalization of cell surface S1PR1 showed that, in the Val124 mutant, pre-bound KSI-6666 was almost completely replaced by the added agonist (Fig. 4c), suggesting that the replacement of Met124 with Val abolished the pseudoirreversible inhibition by KSI-6666. The insurmountable inhibitory activity of KSI-6666 in agonist-induced cAMP production was also significantly impaired in the Val124 mutant, although the effect of the mutation was partial (Fig. 4d) as compared with assay monitoring of the S1PR1 amount (Fig. 4c). This may be attributable to the shorter incubation time in the cAMP production assay. Compared with the mutation to Val, the influence of the replacement of Met124 with Leu was mild (Fig. 4c), which may be consistent with the prediction from MetaD that hydrophobic interaction with the side chain of Met124 contributes to the pseudoirreversible inhibition by KSI-6666.

Met124 is critical for the pseudoirreversible inhibition, and therefore we next focused on the structural basis of the interaction of Met124 with *(R)*-KSI-6666 in MetaD simulation. Further visible inspection of the MetaD trajectories suggested that Met124 may interact with the distal benzene ring of *(R)*-KSI-6666, which has trifluorocarbon (CF_3–) and chloride (Cl–) substituents, rather than with the zwitterionic end of the ligand (Fig. 4a and Supplementary Video 1). To clarify this observation, the distance from Met124 (the γ-carbon atom) to the carbon atom of the CF_3– group was compared with that from Met124 to a hydroxyl oxygen atom of the carboxylic acid in the zwitterionic moiety (hereafter referred to as O1) for the all selected poses in the MetaD trajectories (Fig. 5a). In the original structure determined by the docking study (Fig. 3c),

the distances from Met124 were 10.1 □ for CF_3– and 9.3 □ for O1. A correlation plot of the two distances in the simulation suggested that two major poses were present (named “gate A” and “gate B,” respectively, see Fig. 5a) besides scattered unbound poses. Gate A has a median Met124–CF_3 distance of 9.42 □ and a median Met124–O1 distance of 9.97 □, which is close to the values in the docking structure (yellow asterisk in gate A of Fig. 5a, right). Gate B has a median Met124–CF_3 distance of 6.27 □ and a median Met124–O1 distance of 12.95 □. This suggests that, in the dissociation process of *(R)*-KSI-6666, there is a metastable binding state in which the distal benzene ring in *(R)*-KSI-6666 possessing CF_3– and Cl– substituents becomes close to Met124.

To address if this metastable binding state requires the interaction of Met124 with *(R)*-KSI-6666, we performed the equivalent MetaD simulation for the Val124 mutant. Notably, the frequency of the poses in gate B decreased significantly in the MetaD simulation for the Val124 mutant (Fig. 5a). Overall, a metastable binding state (hereafter referred to as the “Met pocket”) is generated by the interaction of *(R)*-KSI-6666 with Met124, and its formation is correlated with the slow dissociation of *(R)*-KSI-6666 from S1PR1.

We next evaluated the time-dependent transition of *(R)*-KSI-6666 binding poses by plotting the distance between the CF_3– group and Met124 in each run versus time. After starting the MetaD simulation from the docking position, *(R)*-KSI-6666 quickly moved to the Met pocket in seven runs (Runs 1, 3, 4, 7, 8, 9, and 10; Fig. 5b). Subsequently, *(R)*-KSI-6666 dissociated from the Met pocket in three runs (Run 3, 8, and 9); moved to another binding pocket close to the starting position (hereafter referred as to the “deep pocket”) in two runs (Runs 7 and 10); and stayed in the Met pocket in one run (Run 4). In Run 1, although the distal benzene ring moved out of the pocket, *(R)*-KSI-6666 was still bound to S1PR1. In the other three runs (Runs 2, 5 and 6), *(R)*-KSI-6666 was located in the deep pocket soon after starting the simulation. Thereafter, *(R)*-KSI-6666 stayed in the deep pocket in two of the runs (Runs 5 and 6). Finally, in Run 2, *(R)*-KSI-6666 dissociated from the deep pocket. As expected, for the Val124 mutant, *(R)*-KSI-6666 stayed in the deep pocket after starting the simulation and dissociated without entering the Met pocket, except in Run 8, in which it may have been temporarily located in the Met pocket from around 30 to 50 ns (Supplementary Video 3). Overall, these data suggest that Met124 is

involved in the formation of the Met pocket, a metastable binding pocket for *(R)*-KSI-6666 that acts as a "gatekeeper" to limit the dissociation of *(R)*-KSI-6666 from S1PR1.

FMO calculation suggests a contribution of dispersion energy to the interaction between KSI-6666 and Met124 during the dissociation process

To further characterize the Met pocket in S1PR1, the FMO method was applied to estimate the IFIEs of the complexes composed of S1PR1 and *(R)*-KSI-6666 predicted in the MetaD simulations. Because of computational limitations, we selected eight complexes in which *(R)*-KSI-6666 adopted some typical poses interacting with Met124: seven poses from Run 7 (snapshot indexes 601, 618, 628, 633, 646, 661, and 696), which would allow monitoring of the time-dependent change in the interaction energies during the dissociation, and one pose from Run 3 (index 201) (Supplementary Table 2). As shown in the distance plot (Fig. 6a), poses in indexes 601, 661, and 696 were positioned in the deep pocket (gate A in Fig 6a), and those in indexes 201, 618, 628, 633, and 646 were in the Met pocket (gate B in Fig. 6a). The FMO method was applied to these eight complexes to determine IFIEs between *(R)*-KSI-6666 and amino acid residues in S1PR1. On the basis of IFIE values, we performed estimation of Pearson correlation coefficients, clustering and principal component analyses among these eight complexes (Fig. 6b). Interestingly, the poses in the Met pocket (indexes 201, 618, 628, 633, and 646) appeared to be further separated into two groups depending on the IFIEs: the first group included poses in indexes 201 and 618 (early stage in the dissociation), and the second group included poses in indexes 623, 628, and 646 (late stage in the dissociation). In addition, the poses in the deep pocket were also separated into two: a pose in the early stage of the dissociation (index 601), and poses in the late stage of the dissociation (indexes 661 and 696). The total IFIE between *(R)*-KSI-6666 and Met124 was lowest in the group of poses in the Met pocket, especially in the early stage (indexes 201 and 618), suggesting that the interaction between Met124 and *(R)*-KSI-6666 would be enhanced in the Met pocket. Moreover, PIEDA showed that, among DI, CT, and ES energies, the DI energy contributed most to the interaction between *(R)*-KSI-6666 and Met124 (Fig. 6d), which may explain the involvement of hydrophobic interaction in the binding of *(R)*-KSI-6666 and Met124.

The pseudoirreversible inhibition contributes to the persistent efficacy of KSI-6666

The distal benzene ring of *(R)*-KSI-6666 may interact with Met124 in S1PR1 during the dissociation process, and therefore we speculated that a change in the electronic state of the benzene ring may influence the dissociation of the ligand from S1PR1. We then tested the contribution of the substituents on the benzene ring (i.e., CF_3 and Cl, highlighted in Fig. 7a) to the IFIEs between *(R)*-KSI-6666 and Met124. Thus, FMO calculation was re-run for the original complexes with a modification in which the two substituents (CF_3– and Cl–) on the distal benzene ring in *(R)*-KSI-6666 were replaced by hydrogen atoms while the poses of *(R)*-KSI-6666 in S1PR1 were maintained. The calculated IFIE values suggested that the interaction in the Met pocket was weakened (Fig. 7b), whereas that in the deep pocket was increased, in the modified complex (Fig. 7b). In addition, PIEDA calculation suggested that the destabilizing effect in the modified complex was mainly ascribable to DI energy, which reflects the hydrophobic interaction. Consequently, this finding may be consistent with the prediction from the PLIF analysis of MetaD for the involvement of hydrophobic interaction between Met124 and *(R)*-KSI-6666. These data suggest that the CF_3– and Cl– substituents of the distal benzene ring are involved in the binding of *(R)*-KSI-6666 in the Met pocket of S1PR1 by stabilizing the interaction between *(R)*-KSI-6666 and Met124.

We experimentally tested if replacing substituents on the benzene ring with hydrogen atoms influenced the dissociation properties of KSI-6666. Notably, derivative compounds of KSI-6666 lacking the CF_3– substituent (compounds **4** and **5** in Fig. 7a) were almost completely replaced with increased addition of FTY720-P in the functional reversibility assay monitoring the amount of surface S1PR1, suggesting no pseudoirreversible inhibitory activity for these compounds (Fig. 7c), which is consistent with predictions from the FMO calculation. We further tested whether the *in vivo* efficacy of orally administered compounds **4** and **5** was altered compared with that of KSI-6666 by evaluation of their effects on blood leukocyte number. Notably, in contrast to KSI-6666, the reduction of blood leukocytes recovered to the basal level by 32 h after the administration of compound **4** or **5** (Fig. 7c), even though the plasma concentrations of KSI-6666 and compound **4** were comparable (Extended Data Fig. 4), indicating that replacement of the CF_3– group with a hydrogen atom impaired the persistency of the efficacy of KSI-6666. Overall, the data suggest that pseudoirreversible inhibition elicits the persistent efficacy of KSI-

6666 as an S1PR1 antagonist.

Discussion

Slower dissociation of antagonists from receptors elicits longer and more potent inhibition of target molecules *in vivo*[36-39]. For instance, Aprepitant[19], a pseudoirreversible NK1 receptor antagonist used as an antiemetic, potently and persistently inhibited the NK1 receptor *in vivo*. In contrast, the inhibitory effect of a surmountable antagonist CP-99,994 was weaker and lasted for a short period. Our data suggest that KSI-6666 is a new pseudoirreversible inhibitor of S1PR1. Consistently, KSI-6666 showed persistent efficacy *in vivo*. In contrast, W146 appeared not to be a pseudoirreversible inhibitor. In addition to its poor pharmacokinetics, the transient effect of W146 *in vivo* may be in part ascribed to this dissociation property of W146. Our data are consistent with the concept that the slow dissociation of drugs benefits their efficacy[36-39].

The two-step induced fit model may explain the slow dissociation of KSI-6666 from S1PR1. In this model, stable binding of a drug with its target occurs via a two-step mechanism: in the first step, binding to the target forms an encounter complex; then, in the second step, a conformational change of the complex occurs and strengthens the drug binding to the target. In binding via the two-step induced fit mechanism, the residence time of a drug–target complex may be considerably augmented. MetaD simulation of KSI-6666 in the dissociation process from S1PR1 suggested the presence of another stable binding pose requiring residue Met124 (i.e., the “Met pocket”) in addition to the pose close to the original binding pose (i.e., the “deep pocket”). Of note, the replacement of Met124 with Val abolished not only the slow dissociation in the simulation but also the pseudoirreversible inhibition by KSI-6666 *in vitro*. Therefore, KSI-6666 possibly binds to S1PR1 via a two-step induced fit mechanism; it binds to the Met pocket in the first step, and then forms another stable binding structure in the deep pocket, resulting in pseudoirreversible inhibition of S1PR1.

A previous study showed that replacement of Met124 with Lys caused a severe reduction of S1PR1 activity in cell culture. This finding suggests that the hydrophobicity of Met124 is critical for the formation of the binding pocket for the S1PR1 ligand. Our study showed that the replacement of Met124 with Val or Leu did not practically affect the activity of FTY720-P, but severely impaired the slow dissociation of KSI-6666. Thus, Met124 may play roles not only in

the formation of a hydrophobic “wall” for the binding pocket but also as a “gatekeeper” for the binding and unbinding processes of S1PR1 modulators.

The benzene ring moiety in KSI-6666 appears to be critical for the interaction with Met124. S1PR1 modulators can be divided into two types: FTY720-based S1PR1 modulators, which have a flexible lipophilic chain, and structurally divergent ones, most of which have benzene rings[9]. The S1PR1 modulators with benzene rings may use interaction with Met124 to form stable interactions, which results in slow dissociation. Future testing of this hypothesis may help in the design of new S1PR1 antagonists.

Functional antagonists of S1PR1, such as FTY720, have been used for the treatment of MS for more than a decade. In addition to MS, new applications, such as treatment of ulcerative colitis, have been proposed for the S1PR1 agonists, ozanimod and etrasimod[40,41]. In the present study, KSI-6666, a competitive antagonist, showed an efficacy comparable to functional antagonists in rodent colitis models. Accordingly, competitive S1PR1 antagonists with pseudoirreversible inhibition, such as KSI-6666, could potentially be applicable for the treatment of these inflammatory diseases in future.

Computational prediction of drug binding behavior and free energy may be used widely in the development of new drugs in the future. One important issue is to address if computational simulation can predict the actual behavior and efficacy of drugs. In this study, we used molecular dynamics and quantum mechanics methods to explain the structural basis of the pseudoirreversible inhibition of S1PR1 by KSI-6666, and validated the computational predictions in experiments using cell culture and animals. This knowledge regarding the correlation between drug efficiency and the structural basis of the drug dissociation kinetics may help in the design of effective S1PR1 antagonists to suppress inflammatory diseases. In such cases, computer simulation would be helpful for predicting the structural basis of drug binding and unbinding kinetics in addition to equilibrium-binding structures.

Materials and Methods

Chemicals

KSI-6666, *(R)*-KSI-6666, *(S)*-KSI-6666, compounds **1**, **2**, **3**, **4**, and **5**, the Merck S1PR1 agonist, W146, and KRP-203 were synthesized by Kissei Pharmaceutical Co., Ltd. Detailed synthetic schemes and synthetic procedures are presented in the Supplemental Experimental Procedures.

Animals

BALB/cA mice (CLEA Japan and Charles River Laboratories Japan), BALB/cCr mice (Japan SLC), C.B-17 SCID mice (Charles River Laboratories Japan), Sprague-Dawley (SD) rats (Japan SLC), and Hartley guinea pigs (Japan SLC) were maintained in standard controlled conditions with a 12-h lighting cycle and access to chow and water *ad libitum*. Experiments were performed in accordance with the protocols approved by the Laboratory Animal Committee of Kissei Pharmaceutical Co., Ltd. or the Guidelines of the Institutional Animal Care and Use Committee of RIKEN, Yokohama Branch (2018-075). Cynomolgus monkeys (Del Mundo Trading and SICONBREC Inc.) were maintained in standard controlled conditions with a 12-h lighting cycle and access to chow from 9:00 to 13:00 and water *ad libitum*, and experiments were performed by Ina Research Inc. according to protocols approved by the Institutional Animal Care and Use Committee. In total, seven male monkeys were used for the study.

Compound-induced reduction in blood leukocyte count in rats

Compounds dissolved in the vehicle, which consisted of 5%–10% dimethyl sulfoxide (Wako) and 5%–10% Wellsolve (Celeste) mixed in distilled water (Otsuka), were orally administered to 6–16-week-old male SD rats. Blood samples were chronologically collected in EDTA-2K-containing blood collection tubes (BD) under anesthesia before and after compound administration. Leukocytes in blood were counted by an automated hematology analyzer KX-21NV (Sysmex). In some experiments, plasma fractions were isolated and concentrations of compounds were measured by liquid chromatography-mass spectrometry (Q Exactive, Thermo Fisher Scientific).

Induction of lymphopenia in cynomolgus monkeys

Three-to-five-year-old male cynomolgus monkeys were used. The test compound dissolved in vehicle consisting of 0.5% methyl cellulose 400 solution (Wako) and 0.01 M hydrochloric acid (Wako) mixed in distilled water (Otsuka) was orally administered to monkeys. Blood samples were chronologically collected in EDTA-2K-containing blood collection tubes while the monkey was awake, before and after compound administration. Lymphocytes in blood were counted by a using hematology analyzer ADVIA120 (Siemens).

GTP binding assay

Membranes were prepared from HEK293 cells stably transfected with human S1PR1. GTP binding assay was performed using a GTP Gi Binding Assay Kit (Cisbio) according to the manufacturer's protocol. In the antagonist assay, serial dilutions of the test compound and 10 nM Merck S1PR1 selective agonist were coincubated with 1.25 μg/well of cell membranes suspended in the stimulation buffer supplied by the manufacturer containing 50 mM $MgCl_2$ and 2 μM GDP, followed by the addition of GTP Eu Cryptate (donor) and d2 antibody (acceptor). Membranes were incubated overnight at room temperature and the fluorescence signals from the donor (620 nm) and the acceptor (665 nm) were read using a PHERAstar FSX microplate reader (BMG Labtech). The fluorescence ratio (signal 665 nm/signal 629 nm$\times 10^4$) was calculated. The half-maximal inhibitory concentration (IC_{50}) values were calculated by nonlinear regression analysis of the concentration–response curve in GraphPad Prism 6 software. In assays to evaluate the effect of the test compound alone, membranes were treated with serial dilutions of the compound and were subjected to the same operations as noted above. In functional reversibility assays, serial dilutions of the test compound and serial dilutions of FTY720-P were co-incubated with membranes followed by the same operations as noted above. The fluorescence ratio obtained from the response to 10 μM FTY720-P alone was calculated as 100% response (E_{max} = 100%), and that in the condition without FTY720-P or the test compound was defined as 0%. The maximum value of the response to FTY720-P in cotreatment with the test compound (calculated by nonlinear regression analysis of the concentration–response curve in GraphPad Prism 6) was regarded as the E_{max} value.

Receptor internalization assay

HEK293 cells transiently transfected with pBiT3.1-N in which the coding sequence of human S1PR1 was inserted (pBiT3.1-N-WT-S1PR1), resulting in the expression of S1PR1 with an HiBiT-tag at the *N*-terminus, were prepared using Lipofectamine 2000 (Thermo Fisher Scientific). In the functional reversibility assay, serial dilutions of the test compound were preincubated with cells in culture medium consisting of Dulbecco's Modified Eagle's Medium (Wako) supplemented with 10% fetal bovine serum (Biological Industries) for 10 min at 37°C, followed by the induction of receptor internalization by the addition of serial dilutions of FTY720-P (Cayman) or S1P (Cayman). Following 60-min incubation at 37°C, cell surface levels of HiBiT-tagged human S1PR1 were monitored using a Nano Glo HiBiT Extracellular Detection System (Promega) according to the manufacturer's protocol. The surface level of receptors, represented by the luminescence, was read by using a PHERAstar FSX microplate reader. The luminesce induced by 10 μM FTY720-P or 100 μM S1P alone was calculated as 100% response (E_{max} = 100%), and that in the condition without agonist or the test compound was defined as 0%. The maximum value of the response to FTY720-P or S1P following pretreatment of cells with the test compound (calculated by nonlinear regression analysis of the concentration–response curve in GraphPad Prism 6) was regarded as the E_{max} value. In functional reversibility assays with cells expressing mutant S1PR1, pBiT3.1-N with insertion of the mutated human S1PR1 sequence where the original codon for Met124 (ATG) was replaced by GTG or CTG, leading to the expression of M124V (pBiT3.1-N-M124V-S1PR1) or M124V (pBiT3.1-N-M124L-S1PR1), respectively, was transfected into cells. In assays to evaluate the effect of the test compound alone, cells in culture medium were treated with the compound for 60 min at 37°C and the surface S1PR1 levels were evaluated as noted above. In assays to evaluate the antagonistic effect of the test compound, cells in the culture medium were treated with serial dilutions of the compound for 10 min at 37°C, followed by the addition of 10 nM FTY720-P.

Ca^{2+} mobilization assay

CHO-K1 cells transiently transfected with human S1PR2 or S1PR3, or cells transiently co-transfected with human S1PR1, S1PR4, S1PR5, mouse S1PR1, or rat S1PR1 and human Gα15, were prepared using FuGENE HD (Promega). Ca^{2+} mobilization assay using a Fluo-4 Direct Calcium Assay Kit (Thermo Fisher Scientific) was carried out according to the manufacturer's

protocol. Following the pretreatment of Fluo4-loaded cells with serial dilutions of the test compound in an assay buffer consisting of Hanks' Balanced Salt Solution (Thermo Fisher Scientific) and 20 mM HEPES (Thermo Fisher Scientific) supplemented with 0.1% bovine serum albumin (Sigma-Aldrich) and 2.5 mM probenecid (Thermo Fisher Scientific) for 15 min, Ca^{2+} mobilization was induced by 10 nM Merck S1PR1 selective agonist for cells expressing S1PR1, or by 100 nM S1P (Cayman) for human S1PR2-, S1PR3-, S1PR4-, or S1PR5-transfected cells. The increase in cellular calcium level was evaluated using an FDSS 7000 plate reader (Hamamatsu Photonics). IC_{50} values were calculated by nonlinear regression analysis of the concentration–response curve in GraphPad Prism 6 software.

cAMP assay

HEK293 cells transiently transfected with pBiT3.1-N-WT-S1PR1 or pBiT3.1-N-M124V-S1PR1 were prepared using Lipofectamine 2000. Cells were pretreated with serial dilutions of the test compound in assay buffer consisting of Hanks' Balanced Salt Solution, 20 mM HEPES (Thermo Fisher Scientific), and 0.5 mM 3-isobutyl-1-methylxanthine (Wako) for 10 min, followed by the addition of serial dilutions of FTY720-P (Cayman). Following incubation for 10 min, 5 μM forskolin (Wako) was added for 20 min. Cellular cAMP levels were examined using a LANCE Ultra cAMP Kit (PerkinElmer) according to the manufacturer's protocol, and the time-resolved fluorescence resonance energy transfer (TR-FRET) emission (665 nm) was read by using a PHERAstar FSX microplate reader. All procedures were performed at room temperature. The TR-FRET fluorescence obtained from the response to 1 μM FTY720-P alone was calculated as 100% response (E_{max} = 100%) and that in the condition without FTY720-P or the test compound was defined as 0%. The highest value of the response to FTY720-P in cells co-treated with the test compound (calculated by nonlinear regression analysis of the concentration–response curve in GraphPad Prism 6) was regarded as the E_{max} value.

Effect on heart rate in guinea pigs

Six-to-seven-week-old male Hartley guinea pigs anesthetized by intraperitoneal injection of 35 mg/kg pentobarbital sodium (Kyoritsu Seiyaku) and 2.5 mg/kg of butorphanol tartrate (Meiji Seika Pharma) were subjected to tracheotomy after tracheary incision. The thorax was incised, and the carotid artery was catheterized with a PE90 catheter (BD) connected to a blood pressure

amplifier (Nihon Kohden) and heart rate counter (Nihon Kohden) via a DTXPlus Transducer (Merit Medical). Signals were monitored and recorded by using a PowerLab 8/35 instrument (AD Instruments) and LabChart software (AD Instruments). KSI-6666 (30 mg/kg) dissolved in dimethyl sulfoxide was intravenously administered to the animals, followed by intravenous injection of 0.3 mg/kg fingolimod hydrochloride (LC Laboratories) dissolved in dimethyl sulfoxide 15 min after the administration of KSI-6666. The average heart rate counted for 1 min at each time point was used for data analysis.

Chemotaxis assay

Twelve-week-old female BALB/cA mice were sacrificed, and spleens were collected. Splenocytes were prepared after the removal of red blood cells using RBC Lysis Buffer (BioLegend). Cells (2×10^7 cells/mL) in assay medium consisting of phenol red-free RPMI-1640 (Thermo Fisher Scientific) supplemented with 0.1% fatty acid-free bovine serum albumin (Sigma) were incubated with serial dilutions of the test compound for 5 min, and 100 µL cell suspensions were transferred to Transwell inserts (Corning) loaded in 24-well culture plates (BD) filled with 600 µL assay medium per well and 20 nM S1P. Cells were incubated for 3 h at 37°C in a 5% CO_2 incubator, followed by removal of the inserts. Migrated cells in plates were stained with CyQuant (Thermo Fisher Scientific) for 1 h at 37°C in the CO_2 incubator and fluorescence intensity, correlated with cell number, was measured by using a PHERAstar FSX microplate reader.

Flow cytometric analysis of lymphocytes

Compounds were dissolved in 10 mM Na_2CO_3 and 40% (2-hydroxypropyl)-β-cyclodextrin and intraperitoneally administrated to 8-week-old female mice (10 mg/kg). At 1, 2 and 4 h after the administration, whole blood was collected into tubes pretreated with EDTA. After the lysis of erythrocytes by using RBC Lysis Buffer, cell suspensions were stained with anti-mouse CD19 (BD 557399), CD4-PECy7 (BioLegend 100528), and CD8-APCCy7 (BioLegend 100714) antibodies after blocking by anti-CD16/32 antibodies (BioLegend 101302). Dead cells were excluded via 7-aminoactinomycin D staining.

Naïve CD4+CD45Rbhi T cell adoptive transfer colitis model

Eight-to-nine-week-old female BALB/cA mice were sacrificed, and spleens were collected. Splenocytes were prepared after the removal of red blood cells using RBC Lysis Buffer. Naïve T cells were isolated by negative selection using a Mouse Naive T Cell $CD4^+/CD62L^+/CD44^{low}$ Column Kit (R&D Systems). Naïve CD4 T cells were treated with fluorescein isothiocyanate-labeled (FITC) anti-mouse CD45RB antibody (BioLegend), followed by washing. Cells treated with anti-FITC MicroBeads (Miltenyi Biotec) were magnetically separated via a MACS column (Miltenyi Biotec) and $CD4^+CD45RB^{high}$ T cells were thus purified. Cell suspension (6×10^5 cell/mL) was intraperitoneally transferred into 8–10-week-old female C.B-17 SCID mice (500 μL/mouse). Two weeks after the transfer, oral administration of compounds twice daily was started and lasted for 14–16 days. The day after the last administration, the DAI score, consisting of the sum (0–12 points) of the grades for three observations [weight loss (%; none: 0; 0–5: 1; 5–10: 2; 10–20: 3; >20: 4); stool consistency (normal: 0; loose stool: 2; diarrhea: 4); and hematochezia (absence: 0; presence: 4)] was evaluated. Mice were sacrificed and colons were collected, weighed and further evaluations were performed. The histological score, consisting of the sum (0–9 points) of the grades for three observations [decrease in goblet cells (0–3); inflammatory cell infiltration (0–3); and mucosal thickening (0–3)], was determined. For mRNA expression analysis, total RNA was extracted from colons by using an RNeasy Mini Kit (QIAGEN). cDNA was reverse transcribed by using a PrimeScript RT Reagent Kit Perfect Real Time (TaKaRa Bio Inc.). Real-time PCR was performed using a 7500 Fast Real-Time PCR System (Applied Biosystems). SYBR Premix Ex *Taq* Perfect Real Time (TaKaRa Bio Inc.) for S100a9 with a primer set (MA058882) obtained from TaKaRa Bio Inc. and Premix Ex *Taq* Perfect Real Time (TaKaRa Bio Inc.) for 18S rRNA with TaqMan Ribosomal RNA Control Reagents (Applied Biosystems) were used for the reaction. The ΔΔCt method was applied to calculate the relative expression level of target mRNA using the 18S rRNA gene as the reference.

Oxazolone-induced colitis model

A total of 150 μL of 3% 4-ethoxymethylene-2-phenyl-2-oxazolin-5-one (oxazolone; Sigma-Aldrich) dissolved in 100% ethanol (Wako) was applied on shaved back skins of 9–10-week-old male BALB/cCr mice for sensitization. One week after sensitization, 100 μL of 1% oxazolone dissolved in 50% ethanol oxazolone was intrarectally administered to the mice. On the same day,

test compounds were orally administered to mice twice (before and after sensitization). Mice were sacrificed 24 h after sensitization, and colons were collected and weighed. Homogenates of colons were prepared using TisseLyser (QIAGEN) and the amount of interleukin (IL)-4 protein was evaluated using a Mouse IL-4 Quantikine ELISA Kit (R&D Systems).

Molecular docking analysis

Our approach to docking the *(R)*-KSI-6666 molecule to the potential binding sites in S1PR1 used two steps: (1) structure and ligand preparation for docking, and (2) docking of the *(R)*-KSI-6666 molecule. An initial structure of human S1PR1 was modeled from the X-ray structure of S1PR1 with the W146 molecule excluding the *Escherichia* virus T4 structure (PDB: 3v2y)[34] and refined for docking simulations using the Protein Preparation Wizard Script within Maestro[42] (Schrödinger LLC, New York, NY, USA). For the *(R)*-KSI-6666 molecule, ionization and energy minimization were performed by the OPLS3 force field in the LigPrep Script in Maestro. A minimized structure of *(R)*-KSI-6666 was employed as the input structure for docking simulation. To account for both ligand and receptor flexibility in the first step, the Glide 'Induced Fit Docking (IFD)' protocol[43] (Schrödinger LLC) was used, followed by iteratively combining rigid receptor docking using Glide and protein remodeling by side chain searching and minimization using Prime (Schrödinger LLC) techniques. We generated 20 initial orientations of *(R)*-KSI-6666 in a grid box defined by the center of the co-crystalized ligand (W146) using Glide docking [standard precision (SP) mode]. Next, we applied the soften-potential docking options, which involved scaling the van der Waals radii by 0.5 for receptor and *(R)*-KSI-6666 atoms. In the protein remodeling stage, all residues within a 5.0-Å radius of each initial docked *(R)*-KSI-6666 were refined using Prime. *(R)*-KSI-6666 was then redocked into the refined receptor structure using Glide in SP mode. Finally, the best pose for *(R)*-KSI-6666 was rescored according to GlideScore (SP mode). The Docking score of co-crystalized ligand W146 was calculated using the score-in-place procedure of Glide SP mode.

Molecular dynamics and metadynamics simulation

Binding models of *(R)*-KSI-6666 and W146 to the structure of human S1PR1 were examined in 100-ns MetaD simulations using Desmond version 2.3 (Schrödinger LLC). MetaD simulation is a widely used enhanced sampling method that allows the sampling of free energy landscapes. In

this simulation, we defined the biasing collective variables as the distance between the center of mass of the ligands and the ligand-binding residues (Tyr29, Lys34, Tyr98, Asn101, Ser105, Gly106, Thr109, Trp117, Arg120, Glu121, Met124, Phe125, Leu128, Ser192, Val194, Leu195, Pro196, Tyr198, Ile203, Cys206, Thr207, Phe210, Trp269, Leu272, Phe273, Leu276, Glu294, Leu297, Val298, Ala300 and Val301 for *(R)*-KSI-6666; Tyr29, Lys34, Tyr98, Asn101, Ser105, Gly106, Thr109, Trp117, Arg120, Glu121, Met124, Phe125, Leu128, Thr193, Val194, Leu195, Pro196, Ile203, Cys206, Thr207, Phe210, Trp269, Leu272, Phe273, Leu276, Glu294, Leu297, Ala300 and Val301 for W146). The initial Gaussian hill height was set at 0.3. The OPLS3e force field[44,45] was used for the simulations. The human S1PR1 structure was placed in a large palmitoyl-oleoyl-phosphatidylcholine (POPC) bilayer, and transferable intermolecular potential 3 point (TIP3P) water molecules were solvated with 0.15 M NaCl. After minimization and relaxation of the model, the production molecular dynamics phase was performed for 10 independent 100-ns simulations in the isothermal–isobaric (NPT) ensemble at 300 K and 1 bar using a Langevin thermostat. The long-range electrostatic interactions were computed using the Smooth Particle Mesh Ewald method. All system setups were performed using Maestro. The MetaD procedure for *(R)*-KSI-6666 in the M124V variant was identical to that for wild-type S1PR1. The model of M124V S1PR1 was constructed using Maestro.

Protein–ligand interaction fingerprint analysis

PLIF analyses from MetaD trajectories were performed using the PLIF modules of MOE 2020.0901 (Chemical Computing Group Inc., Montreal, Quebec, Canada). Energy-based contacts, including side chain hydrogen bonds (donor or acceptor), backbone hydrogen bonds (donor or acceptor), solvent hydrogen bonds (donor or acceptor), ionic interactions, metal binding interactions, and π interactions, and surface contact fingerprints, were employed. After the PLIFs had been generated based on 1000 snapshot structures (every 1 ns in 10 independent 100-ns simulations) for each ligand, the probability of each bit occurring for each residue for *(R)*-KSI-6666 compared with W146 was calculated as Qb.

$$Q_b = \frac{C_b}{C_0} \cdot 2\left(P_b - \frac{1}{2}\right)$$

where Cb is the number of snapshots within the set that have the fingerprint bit set, and C0 is the total number of snapshots. Pb is the relative probability of the fingerprint bit entry over the snapshots for *(R)*-KSI-6666 compared with that for W146 if it contains the bit. Qb takes values

from −1 to 1. A higher positive value indicates a higher probability of the bit occurring for *(R)*-KSI-6666.

Fragment molecular orbital method

The initial complex structure of the *(R)*-KSI-6666-bound S1PR1 and selected structures from trajectories in MetaD simulation for *(R)*-KSI-6666 dissociation were minimized using the Impref module (Schrödinger LLC) with the OPLS3e force field. To evaluate the contribution of the two substituents (CF_3 and Cl) on the distal benzene ring of *(R)*-KSI-6666, an additional complex in which the original *(R)*-KSI-6666 was modified by replacing both substituents with hydrogen atoms was also generated. FMO calculation[46] was then performed using the ABINIT-MP program[47] at the FMO2-MP2/6-31G(d) level and IFIE with PIEDA was calculated using MIZUHO/BioStation viewer.

Conflict of Interest

YM, YOh, TS, YY, KO, HI, AY, MH, and YOk are employees of Kissei Pharmaceutical Co., Ltd.

Acknowledgement

This work was supported by the Research Support Project for Life Science and Drug Discovery (Basis for Supporting Innovative Drug Discovery and Life Science Research [BINDS]) from AMED (grant number JP22ama121029j0001 to T.H.), Grants-in-Aid for Scientific Research from JSPS (17H04038, 17K08622, 20K07332, and 20H03441 to T.A. and N.A.), Grants-in-Aid for Scientific Research in Innovative Areas from MEXT (18H04989 and 19H04821 to T.A. and N.A.) and by CREST from the Japan Science and Technology Agency (JPMJCR2011 to T.A.). The authors declare no competing financial interests. We thank Edanz (https://jp.edanz.com/ac) for editing a draft of this manuscript.

Author contributions

YM, YOh, TS, MM, TM, and NA performed the experiments. KO and HI synthesized the chemicals. AY performed LC-MS analysis. MH and YOk performed histological analysis. YY and TH performed *in silico* calculations. YM, YY, TI, KH, MH, TH, and TA analyzed the MetaD and FMO data. YM and TA designed the study and wrote the paper.

Figure legends

Figure 1. KSI-6666 persistently antagonizes S1PR1.

a. Lead optimization of S1PR1 antagonists with long-lasting efficacy. Structures of compounds synthesized for sequential optimization are shown. The IC_{50} value in GTP binding assay using the membrane fraction of HEK293 cells stably expressing human S1PR1 was calculated. S1PR1 was activated by 10 nM Merck S1PR1 agonist. Data were obtained from three independent experiments (mean ± s.e.m.). The chiral carbon atom in KSI-6666 is indicated by an asterisk.

b. Effect of KSI-6666 and compounds **2** and **3** on leukocyte number in blood of rats. Each compound was orally administered to Sprague Dawley (SD) rats at 3 mg/kg. Leukocytes in the blood were counted at the indicated times. Leukocyte number was normalized as a percentage from the baseline count before administration (mean ± s.e.m., n = 4–6 /group). Statistical analyses compared with KSI-6666 were performed by two-way analysis of variance (ANOVA).

c. Effect of KSI-6666, FTY720-phosphate (FTY720-P), and Merck S1PR1 agonist on GTP binding activity in HEK293 cells expressing S1PR1. Data were obtained from three independent experiments (mean ± s.e.m.).

d. Effect of KSI-6666, FTY720-P, and W146 on the level of S1PR1 on the surface of HEK293 cells. Data were obtained from three independent experiments (mean ± s.e.m.).

e. Effect of KSI-6666 on Ca^{2+} mobilization induced by the activation of S1P receptor subtypes. Ca^{2+} mobilization was induced by 10 nM S1PR1 agonist (for S1PR1 of human, mouse, or rat), or by 100 nM S1P (for human S1PR2, S1PR3, S1PR4, or S1PR5) in CHO-K1 cells expressing S1P receptors. Gα15 was co-expressed with S1PR1, S1PR4, or S1PR5 to enable signaling from these receptors to phospholipase C. The IC_{50} value of the test compound was calculated. Data are the mean ± s.e.m. of three independent experiments.

f. Effect of KSI-6666 pretreatment on downregulation of surface S1PR1 induced by FTY720-P. HEK293 cells expressing S1PR1 were treated with KSI-6666 at the indicated concentrations. w/o indicates no treatment with KSI-6666. Data were obtained from three independent experiments (mean ± s.e.m.).

g. Effect of KSI-6666 pretreatment on the FTY720-P-induced reduction in the heart rate of guinea pigs. Heart rate over time was measured for 45 min in total (mean ± s.e.m., n = 3 /group). Statistical analysis was performed by two-way ANOVA.

h. Effect of KSI-6666 pretreatment on the FTY720-P-induced chemotactic activity of splenocytes. Transwell assay was performed using murine splenocytes. Data are the mean ± s.e.m. of the results from three mice. Statistical analysis *vs*. treatment with S1P alone was performed by one-way ANOVA followed by Dunnett's test.

i. Effect of KSI-6666 and W146 on blood lymphocytes in mice. After each drug was intravenously administrated (10 mg/kg), frequency and cell numbers of $CD4^+$, $CD8^+$, and $CD19^+$ cells were analyzed by flow cytometry. n = 6 each for 1 and 4 h, n = 9 for the control (0 h). P values (two-tailed Student's t test) were indicated in the figure.

j. Effect of KSI-6666 on lymphocyte number in blood of cynomolgus monkeys. KSI-6666 was orally administered to monkeys at 3 mg/kg. Lymphocytes in the blood were counted at the indicated times. Lymphocyte number was normalized as a percentage from the baseline count before administration (mean ± s.e.m., n = 3 /group). Statistical analysis *vs*. vehicle was performed by two-way ANOVA.

Figure 2. KSI-6666 is a potent anti-inflammatory agent.

a. Therapeutic efficacies of KSI-6666 (15 mg/kg b.i.d.) and KRP-203 (1.5 mg/kg b.i.d.) in T-cell transfer colitis model. Isolated naive $CD4^+CD45RB^{high}$ T cells from BALB/cA mice were injected intraperitoneally into SCID mice and colitis was elicited. Two weeks after the transfer, twice daily oral administration of each compound was started and lasted for 14–16 days. Animals were sacrificed on the day after the final administration. Colon weight, disease activity index (DAI) score, histological score, and *S100a9* mRNA expression level relative to ribosomal RNA expression were evaluated in each group. Statistical analysis was performed by either Student's *t*-test or Welch's *t*-test according to F-test results (mean ± s.e.m., n = 15–35 /group).

b. A representative example of the histology.

c. Efficacies of KSI-6666 (15 mg/kg b.i.d.) and KRP-203 (1.5 mg/kg b.i.d.) in oxazolone-induced colitis model. Oxazolone (3% solution) was applied on back skins of BALB/cA mice on day 1 (sensitization), followed by intrarectal administration of 1% oxazolone on day 8 (challenge), and colitis was elicited. Each test compound was orally administered twice on day 8 and animals were sacrificed on day 9. Colon weight and interleukin (IL)-4 protein amount in the colon in each group were evaluated and the percentage of controls (colitis-induced mice to which vehicle was administered) was calculated. Statistical analysis was performed by either Student's *t*-test or Welch's *t*-test according to F-test results (mean ± s.e.m., n = 9–19).

Figure 3. KSI-6666 is a pseudoirreversible inhibitor.

a. Difference between KSI-6666 enantiomers in inhibitory activities against GTP binding to S1PR1 induced by 10 nM Merck S1PR1 agonist. Data were obtained from three independent experiments. Results are expressed as the mean ± s.e.m. Magenta line, *(RS)*-KSI-6666; cyan line, *(R)*-KSI-6666; green line, *(S)*-KSI-6666.

b. Effect of *(RS)*-KSI-6666, *(R)*-KSI-6666, and *(S)*-KSI-6666 on leukocyte number in blood of rats. Each compound was orally administered to SD rats at 3 mg/kg. Leukocytes in the blood were counted at the indicated times. Leukocyte number was normalized as a percentage from the baseline count before the administration (mean ± s.e.m., n = 3 /group).

c. Docking pose of *(R)*-KSI-6666 (left) and crystallographic pose of W146 (middle) with S1PR1. In the merge figure, *(R)*-KSI-6666 and W146 are depicted in green and gray, respectively.

d. Interfragment interaction energies (IFIEs) between *(R)*-KSI-6666 and amino acids in S1PR1. IFIEs below −2 kcal/mol are shown in the figure. The results of pair interaction energy decomposition analysis are shown as green bars for electrostatic energies (ES), red bars for dispersion energies (DI), orange bars for charge transfer and mix energies (CT+ mix), and blue bars for exclusion energies (EX).

e. Plots of binding free energy profiles (kcal/mol) against the distance between the center of mass of the ligand-binding residues and the ligand in metadynamics (MetaD) trajectories for *(R)*-KSI-6666 (left) and W146 (right) in the dissociation pathway from S1PR1. The results from all 10 simulation runs are plotted for each compound.

f. Plots of ligand root-mean-square deviation against simulation time in the MetaD trajectories for *(R)*-KSI-6666 (left) and W146 (right) in the dissociation pathways from S1PR1. The results from all 10 runs are plotted for each compound.

g. Functional reversibility of KSI-6666 and W146 examined by agonist-induced S1PR1 internalization assay. HEK293 cells expressing HiBiT-tagged human S1PR1 were treated with each compound and concentration-dependent S1PR1 internalization induced by FTY720-P (upper left) or S1P (lower left), represented by luciferase activity, was measured. Calculated E_{max} values for the FTY720-P (upper right) and S1P (lower right)-induced response on treatment with each compound at different concentrations. Data for the upper and lower graphs were obtained from five and three independent experiments, respectively. Statistical analysis was performed by one-way ANOVA, followed by Tukey's test for KSI-6666. Results are expressed

as the mean ± s.e.m.

h. Functional reversibility of KSI-6666 and W146 examined by agonist-induced GTP binding assay (upper). Calculated E_{max} values for the FTY720-P-induced response on treatment with each compound at different concentrations (lower). Data were obtained from eight independent experiments. Statistical analysis was performed by one-way ANOVA, followed by Tukey's test for KSI-6666 (n = 4–8 /condition of antagonist treatment, mean ± s.e.m.).

Figure 4. Met124 of S1PR1 is critical for pseudoirreversible inhibition by KSI-6666.

a. Typical poses of *(R)*-KSI-6666 in the ligand binding pocket of S1PR1 in MetaD simulation. Residues Thr207, Phe210, and Phe273, representing the inner pocket, are shown in line style, and Met124 is shown in CPK style.

b. Significant protein–ligand interactions of *(R)*-KSI-6666 relative to W146 in protein–ligand interaction fingerprint (PLIF) analysis. The interaction between the compound and S1PR1 during MetaD simulation was represented in a fingerprint scheme by the PLIF tool. The interaction between the compound and each amino acid residue of S1PR1 was evaluated in two main categories: potential-energy based contacts and surface contacts. When an interaction above a threshold was observed for the residue, a fingerprint bit representing the interaction was assigned. Hydrogen bonding, ionic interaction, and π interaction (arene attraction) were identified as potential contacts with energies >0.5 kcal/mol and assigned as fingerprint bits in this analysis. For hydrogen bonding, each amino acid residue was broken down into side chain (SC) and backbone (BB) categories, and each was classified as either electron donor or acceptor. When a surface contact with area >15 $\square^2$ was observed, a fingerprint bit was assigned. The probability of each bit occurring for each residue for *(R)*-KSI-6666 compared with W146 was calculated as Qb, where Qb takes values from −1 to 1. A higher positive value indicates a higher probability of the bit occurring for *(R)*-KSI-6666. The columns show the value of Qb for each residue. The fingerprint bits shown are total surface contacts (left); and arene attraction (representing π interaction), ionic attraction, and BB hydrogen acceptor, BB hydrogen donor, SC hydrogen acceptor, and SC hydrogen donor interactions with *(R)*-KSI-6666 (right, different interactions shown in different colors).

c. Functional reversibility of KSI-6666 with Val124 and Leu124 mutants of S1PR1 examined by the S1PR1 internalization assay. HEK293 cells expressing HiBiT-tagged human S1PR1 Val124

mutant (M124V, left) or Leu124 mutant (M125L, middle) were treated with KSI-6666 and concentration-dependent receptor internalization stimulated by FTY720-P was measured. Calculated E_{max} values for the FTY720-P-induced response on treatment with KSI-6666 at different concentrations are plotted for wild-type S1PR1 and the two mutants (right). The plot for the wild-type shown in Fig. 3g is reiterated here as a control. Data for the Val124 and Leu124 mutants were obtained from four and three independent experiments, respectively. Statistical analyses *vs*. wild-type were performed by two-way ANOVA for the Val124 and Leu124 mutants. Results are expressed as the mean ± s.e.m.

d. cAMP assay evaluating the functional reversibility of KSI-6666 in wild-type S1PR1 and the Val124 mutant. HEK293 cells expressing HiBiT-tagged wild-type S1PR1 (left) or the Val124 mutant (middle) were treated with KSI-6666 and concentration-dependent inhibition by FTY720-P of forskolin-induced cAMP production was measured. Calculated E_{max} values for the FTY720-P-induced response on treatment with KSI-6666 at different concentrations are plotted for the wild-type and the mutant (right). Data were obtained from three independent experiments, respectively. Statistical analysis was performed by two-way ANOVA. Results are expressed as the mean ± s.e.m.

Figure 5. Metadynamics simulation suggests the presence of a metastable binding pocket for KSI-6666 in S1PR1.

a. Plot of distance from Met124 (γ-carbon atom) to the carbon atom of the CF_3– group on the distal benzene ring of *(R)*-KSI-6666 against the distance from Met124 to the carboxylic acid (O1 atom) of *(R)*-KSI-6666 in MetaD snapshots of wild-type S1PR1 (left) and the Val124 mutant (middle). Snapshots (*n* = 1000) were selected every 1 ns from 10 independent 100-ns MetaD simulations for each form of S1PR1. The area where both distances were <25 □ is enlarged in the right-hand figure. The frequency of poses assigned to gate A (distance between Met124 or Val124 and the carbon atom of the CF_3– group 2.5–7.8 □, distance between Met124 or Val124 and the oxygen atom of the carboxylic acid 10–15 □) and gate B (distance between Met124 or Val124 and the carbon atom of the CF_3– group 7.8–12.5 □, distance between Met124 or Val124 and the oxygen atom of the carboxylic acid, 7.5–12.5 □) is shown for the wild-type (blue) and Val124 mutant (red) proteins.

b. Time-dependent changes in the distance between the carbon atom of the CF_3– group of *(R)*-KSI-6666 and the γ-carbon atom of Met124 (left) or Val124 (right) of S1PR1. The results of all runs are shown in the upper figures. The results of runs in which the binding of *(R)*-KSI-6666 lasted for at least 100 ns are extracted in the lower figures.

Figure 6. Fragment molecular orbital (FMO) calculation suggested the interaction of *(R)*-KSI-6666 and Met124 is strengthened in a metastable binding pocket.

a. Plot of distance from Met124 (γ-carbon atom) of S1PR1 to the carbon atom of the CF_3– group on the distal benzene ring of *(R)*-KSI-6666 against distance from Met124 to the carboxylic acid (O1 atom) of *(R)*-KSI-6666 corresponding to the poses selected for FMO calculation. Snapshot indexes selected are shown. The plot corresponding to the docked structure is indicated by an orange circle.

b. Pearson correlation and clustering of poses based on total interaction energy calculated by the FMO method using complexes of *(R)*-KSI-6666 and S1PR1.

c. Principal component analysis of poses based on total interaction energy calculated by the FMO method using complexes of *(R)*-KSI-6666 and S1PR1.

d. IFIEs of *(R)*-KSI-6666 with Met124 in each group of poses. The snapshot index to which each pose belongs is shown above the bar chart. The average IFIE of poses in the group is

shown.

Figure 7. Derivative compounds of KSI-6666 that lack pseudoirreversible inhibition have poor persistent efficacy.

a. Structures of KSI-6666 and related compounds **4** and **5**.

b. Differential IFIEs of modified and original complexes. The complex of *(R)*-KSI-6666 and Met124 was modified by replacing the two substituents on the distal benzene ring of *(R)*-KSI-6666 (i.e., CF_3 and Cl) with hydrogen atoms. The two complexes were subjected to FMO calculation and the differences between their IFIEs were calculated. The pose index for each group is shown above the bar chart. The average IFIE of poses was employed.

c. Functional reversibility of compounds **4** and **5** examined by S1PR1 internalization assay. HEK293 cells expressing HiBiT-tagged human S1PR1 were treated with compound **4** (left) or **5** (middle) and concentration-dependent receptor internalization stimulated by FTY720-P was measured. Calculated E_{max} values for the FTY720-P-induced response on treatment with these compounds at different concentrations are plotted (right). The plot of KSI-6666 data shown in Fig. 3g (upper right) is reiterated as a control. Data for compounds **4** and **5** were obtained from three independent experiments for each. Statistical analyses *vs*. KSI-6666 were performed by two-way ANOVA for compounds **4** and **5**. Results are expressed as the mean ± s.e.m.

d. *In vivo* efficacy of KSI-6666, and compounds **4** and **5**. Each compound was orally administered to SD rats at the dose indicated and the efficacy, represented as the magnitude of reduction in blood leukocyte count, was evaluated at the indicated times after administration (left). Leukocyte number was normalized as a percentage from the baseline count before administration. Data for a single individual belonging to the control shown in Fig. 1b are reiterated for comparison. Statistical analyses *vs*. KSI-6666 were performed by two-way ANOVA for compounds **4** and **5**. Results are expressed as the mean ± s.e.m. (n = 4–8 /group). Corresponding plasma concentrations of KSI-6666 and compound **4** at two time points are shown in the right-hand graph (mean ± s.e.m.).

References

1. Cartier, A. & Hla, T. Sphingosine 1-phosphate: Lipid signaling in pathology and therapy. *Science* **366**(2019).
2. Chun, J., Kihara, Y., Jonnalagadda, D. & Blaho, V.A. Fingolimod: Lessons Learned and New Opportunities for Treating Multiple Sclerosis and Other Disorders. *Annu Rev Pharmacol Toxicol* **59**, 149-170 (2019).
3. Brinkmann, V. et al. Fingolimod (FTY720): discovery and development of an oral drug to treat multiple sclerosis. *Nat Rev Drug Discov* **9**, 883-97 (2010).
4. Jozefczuk, E., Guzik, T.J. & Siedlinski, M. Significance of sphingosine-1-phosphate in cardiovascular physiology and pathology. *Pharmacol Res* **156**, 104793 (2020).
5. Camm, J., Hla, T., Bakshi, R. & Brinkmann, V. Cardiac and vascular effects of fingolimod: mechanistic basis and clinical implications. *Am Heart J* **168**, 632-44 (2014).
6. Fryer, R.M. et al. The clinically-tested S1P receptor agonists, FTY720 and BAF312, demonstrate subtype-specific bradycardia (S1P(1)) and hypertension (S1P(3)) in rat. *PLoS One* **7**, e52985 (2012).
7. Sanna, M.G. et al. Enhancement of capillary leakage and restoration of lymphocyte egress by a chiral S1P1 antagonist in vivo. *Nat Chem Biol* **2**, 434-41 (2006).
8. Tarrason, G. et al. The sphingosine-1-phosphate receptor-1 antagonist, W146, causes early and short-lasting peripheral blood lymphopenia in mice. *Int Immunopharmacol* **11**, 1773-9 (2011).
9. Marciniak, A., Camp, S.M., Garcia, J.G.N. & Polt, R. An update on sphingosine-1-phosphate receptor 1 modulators. *Bioorg Med Chem Lett* **28**, 3585-3591 (2018).
10. Quancard, J. et al. A potent and selective S1P(1) antagonist with efficacy in experimental autoimmune encephalomyelitis. *Chem Biol* **19**, 1142-51 (2012).
11. Copeland, R.A., Pompliano, D.L. & Meek, T.D. Drug-target residence time and its implications for lead optimization. *Nat Rev Drug Discov* **5**, 730-9 (2006).
12. Copeland, R.A. The drug-target residence time model: a 10-year retrospective. *Nat Rev Drug Discov* **15**, 87-95 (2016).
13. Tautermann, C.S. Impact, determination and prediction of drug-receptor residence times for GPCRs. *Curr Opin Pharmacol* **30**, 22-26 (2016).
14. Bernetti, M., Cavalli, A. & Mollica, L. Protein-ligand (un)binding kinetics as a new

paradigm for drug discovery at the crossroad between experiments and modelling. *Medchemcomm* **8**, 534-550 (2017).

15. Sykes, D.A. et al. Extrapyramidal side effects of antipsychotics are linked to their association kinetics at dopamine D2 receptors. *Nat Commun* **8**, 763 (2017).
16. Sykes, D.A. et al. Fevipiprant (QAW039), a Slowly Dissociating CRTh2 Antagonist with the Potential for Improved Clinical Efficacy. *Mol Pharmacol* **89**, 593-605 (2016).
17. Agren, R. et al. Ligand with Two Modes of Interaction with the Dopamine D2 Receptor-An Induced-Fit Mechanism of Insurmountable Antagonism. *ACS Chem Neurosci* **11**, 3130-3143 (2020).
18. Vauquelin, G., Van Liefde, I., Birzbier, B.B. & Vanderheyden, P.M. New insights in insurmountable antagonism. *Fundam Clin Pharmacol* **16**, 263-72 (2002).
19. Hale, J.J. et al. Structural optimization affording 2-(R)-(1-(R)-3, 5-bis(trifluoromethyl)phenylethoxy)-3-(S)-(4-fluoro)phenyl-4- (3-oxo-1,2,4-triazol-5-yl)methylmorpholine, a potent, orally active, long-acting morpholine acetal human NK-1 receptor antagonist. *J Med Chem* **41**, 4607-14 (1998).
20. Tiwary, P., Limongelli, V., Salvalaglio, M. & Parrinello, M. Kinetics of protein-ligand unbinding: Predicting pathways, rates, and rate-limiting steps. *Proc Natl Acad Sci U S A* **112**, E386-91 (2015).
21. Buch, I., Giorgino, T. & De Fabritiis, G. Complete reconstruction of an enzyme-inhibitor binding process by molecular dynamics simulations. *Proc Natl Acad Sci U S A* **108**, 10184-9 (2011).
22. Tiwary, P., Mondal, J. & Berne, B.J. How and when does an anticancer drug leave its binding site? *Sci Adv* **3**, e1700014 (2017).
23. Kokh, D.B. et al. Estimation of Drug-Target Residence Times by tau-Random Acceleration Molecular Dynamics Simulations. *J Chem Theory Comput* **14**, 3859-3869 (2018).
24. Cavalli, A., Spitaleri, A., Saladino, G. & Gervasio, F.L. Investigating drug-target association and dissociation mechanisms using metadynamics-based algorithms. *Acc Chem Res* **48**, 277-85 (2015).
25. Callegari, D. et al. Metadynamics Simulations Distinguish Short- and Long-Residence-Time Inhibitors of Cyclin-Dependent Kinase 8. *J Chem Inf Model* **57**, 159-169 (2017).

26. Decherchi, S. & Cavalli, A. Thermodynamics and Kinetics of Drug-Target Binding by Molecular Simulation. *Chem Rev* **120**, 12788-12833 (2020).
27. Sledz, P. & Caflisch, A. Protein structure-based drug design: from docking to molecular dynamics. *Curr Opin Struct Biol* **48**, 93-102 (2018).
28. Laio, A. & Parrinello, M. Escaping free-energy minima. *Proc Natl Acad Sci U S A* **99**, 12562-6 (2002).
29. Heifetz, A. et al. Analyzing GPCR-Ligand Interactions with the Fragment Molecular Orbital (FMO) Method. *Methods Mol Biol* **2114**, 163-175 (2020).
30. Heifetz, A., James, T., Southey, M., Bodkin, M.J. & Bromidge, S. Guiding Medicinal Chemistry with Fragment Molecular Orbital (FMO) Method. *Methods Mol Biol* **2114**, 37-48 (2020).
31. Ibrahim, M.A. et al. Discovery of a novel class of potent and orally bioavailable sphingosine 1-phosphate receptor 1 antagonists. *J Med Chem* **55**, 1368-81 (2012).
32. Stewart, G.D., Sexton, P.M. & Christopoulos, A. Inverse Agonists. in *Encyclopedia of Psychopharmacology* (ed. Stolerman, I.P.) 661-667 (Springer Berlin Heidelberg, Berlin, Heidelberg, 2010).
33. Shimizu, H. et al. KRP-203, a novel synthetic immunosuppressant, prolongs graft survival and attenuates chronic rejection in rat skin and heart allografts. *Circulation* **111**, 222-9 (2005).
34. Hanson, M.A. et al. Crystal structure of a lipid G protein-coupled receptor. *Science* **335**, 851-5 (2012).
35. Guo, D., Hillger, J.M., AP, I.J. & Heitman, L.H. Drug-target residence time--a case for G protein-coupled receptors. *Med Res Rev* **34**, 856-92 (2014).
36. Dahl, G. & Akerud, T. Pharmacokinetics and the drug-target residence time concept. *Drug Discov Today* **18**, 697-707 (2013).
37. Lu, H. & Tonge, P.J. Drug-target residence time: critical information for lead optimization. *Curr Opin Chem Biol* **14**, 467-74 (2010).
38. Guo, D., Mulder-Krieger, T., AP, I.J. & Heitman, L.H. Functional efficacy of adenosine A(2)A receptor agonists is positively correlated to their receptor residence time. *Br J Pharmacol* **166**, 1846-59 (2012).
39. Schneider, E.V., Bottcher, J., Huber, R., Maskos, K. & Neumann, L. Structure-kinetic

relationship study of CDK8/CycC specific compounds. *Proc Natl Acad Sci U S A* **110**, 8081-6 (2013).

40. Sandborn, W.J. et al. Ozanimod as Induction and Maintenance Therapy for Ulcerative Colitis. *N Engl J Med* **385**, 1280-1291 (2021).

41. Sandborn, W.J. et al. Efficacy and Safety of Etrasimod in a Phase 2 Randomized Trial of Patients With Ulcerative Colitis. *Gastroenterology* **158**, 550-561 (2020).

42. Sastry, G.M., Adzhigirey, M., Day, T., Annabhimoju, R. & Sherman, W. Protein and ligand preparation: parameters, protocols, and influence on virtual screening enrichments. *J Comput Aided Mol Des* **27**, 221-34 (2013).

43. Sherman, W., Day, T., Jacobson, M.P., Friesner, R.A. & Farid, R. Novel procedure for modeling ligand/receptor induced fit effects. *J Med Chem* **49**, 534-53 (2006).

44. Roos, K. et al. OPLS3e: Extending Force Field Coverage for Drug-Like Small Molecules. *J Chem Theory Comput* **15**, 1863-1874 (2019).

45. Kurki, M., Poso, A., Bartos, P. & Miettinen, M.S. Structure of POPC Lipid Bilayers in OPLS3e Force Field. *J Chem Inf Model* (2022).

46. Kitaura, K., Ikeo, E., Asada, T., Nakano, T. & Uebayasi, M. Fragment molecular orbital method: an approximate computational method for large molecules. *Chemical Physics Letters* **313**, 701-706 (1999).

47. Starikov, E.B. et al. *Modern methods for theoretical physical chemistry of biopolymers*, (Elsevier, Amsterdam ; Boston, 2006).

Figure 1

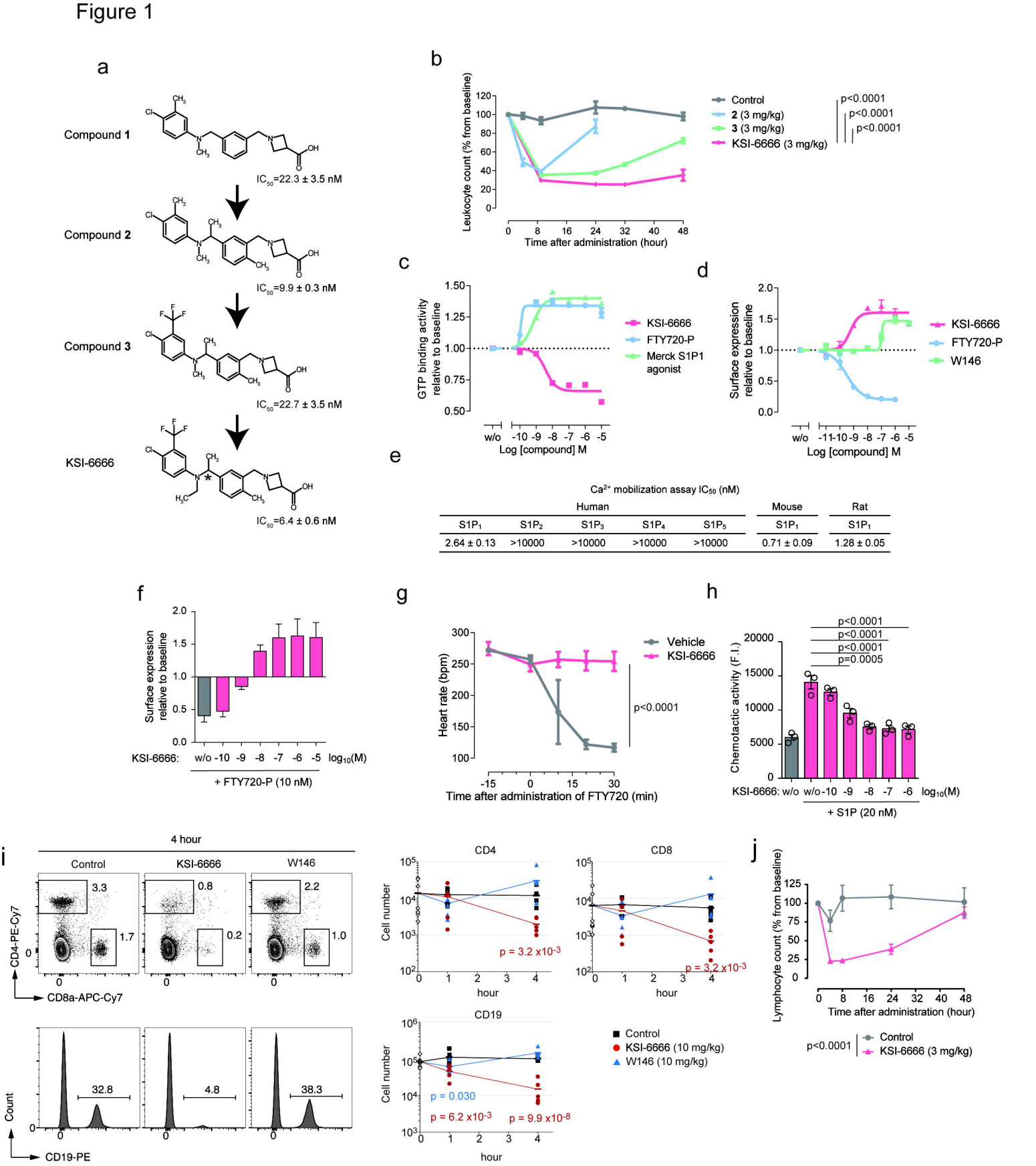
a
Compound 1
IC50=22.3 ± 3.5 nM
Compound 2
IC50=9.9 ± 0.3 nM
Compound 3
IC50=22.7 ± 3.5 nM
KSI-6666
IC50=6.4 ± 0.6 nM
b
Leukocyte count (% from baseline)
Time after administration (hour)
Control
2 (3 mg/kg)
3 (3 mg/kg)
KSI-6666 (3 mg/kg)
p<0.0001
p<0.0001
p<0.0001
c
GTP binding activity relative to baseline
Log [compound] M
KSI-6666
FTY720-P
Merck S1P1 agonist
d
Surface expression relative to baseline
Log [compound] M
KSI-6666
FTY720-P
W146
e
Ca2+ mobilization assay IC50 (nM)
Human
Mouse
Rat
S1P1 S1P2 S1P3 S1P4 S1P5
S1P1
S1P1
2.64 ± 0.13 >10000 >10000 >10000 >10000
0.71 ± 0.09
1.28 ± 0.05
f
Surface expression relative to baseline
KSI-6666: w/o -10 -9 -8 -7 -6 -5 log10(M)
+ FTY720-P (10 nM)
g
Heart rate (bpm)
Time after administration of FTY720 (min)
Vehicle
KSI-6666
p<0.0001
h
Chemotactic activity (F.I.)
p<0.0001
p<0.0001
p<0.0001
p=0.0005
KSI-6666: w/o w/o -10 -9 -8 -7 -6 log10(M)
+ S1P (20 nM)
i
4 hour
Control
KSI-6666
W146
CD4-PE-Cy7
CD8a-APC-Cy7
3.3
1.7
0.8
0.2
2.2
1.0
Count
CD19-PE
32.8
4.8
38.3
CD4
CD8
CD19
Cell number
hour
p = 3.2 x10-3
p = 3.2 x10-3
p = 0.030
p = 6.2 x10-3
p = 9.9 x10-8
Control
KSI-6666 (10 mg/kg)
W146 (10 mg/kg)
j
Lymphocyte count (% from baseline)
Time after administration (hour)
p<0.0001
Control
KSI-6666 (3 mg/kg)

Figure 2

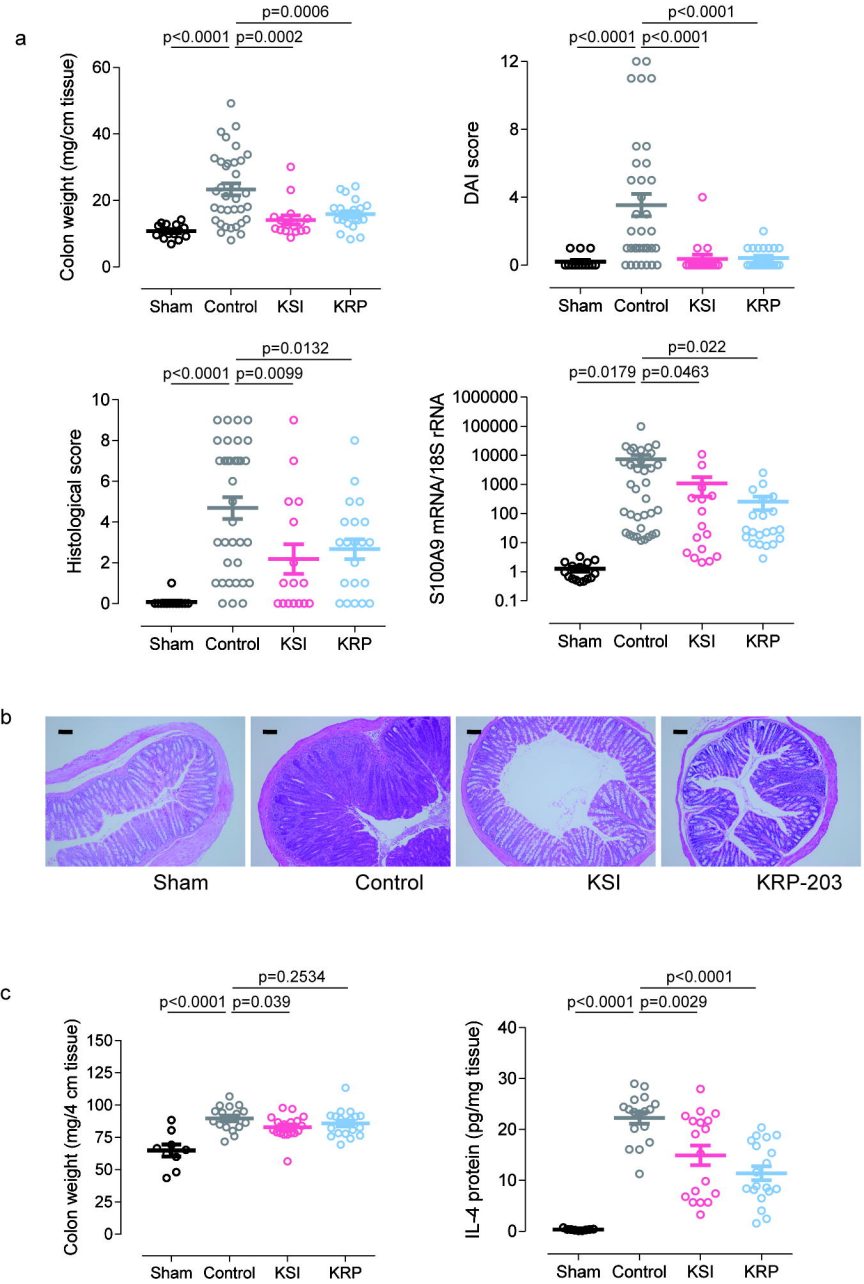
a
p=0.0006
p<0.0001
p=0.0002
Colon weight (mg/cm tissue)
60
40
20
0
Sham
Control
KSI
KRP
p<0.0001
p<0.0001
p<0.0001
DAI score
12
8
4
0
Sham
Control
KSI
KRP
p=0.0132
p<0.0001
p=0.0099
Histological score
10
8
6
4
2
0
Sham
Control
KSI
KRP
p=0.022
p=0.0179
p=0.0463
S100A9 mRNA/18S rRNA
1000000
100000
10000
1000
100
10
1
0.1
Sham
Control
KSI
KRP
b
Sham
Control
KSI
KRP-203
c
p=0.2534
p<0.0001
p=0.039
Colon weight (mg/4 cm tissue)
150
125
100
75
50
25
0
Sham
Control
KSI
KRP
p<0.0001
p<0.0001
p=0.0029
IL-4 protein (pg/mg tissue)
40
30
20
10
0
Sham
Control
KSI
KRP

Figure 3

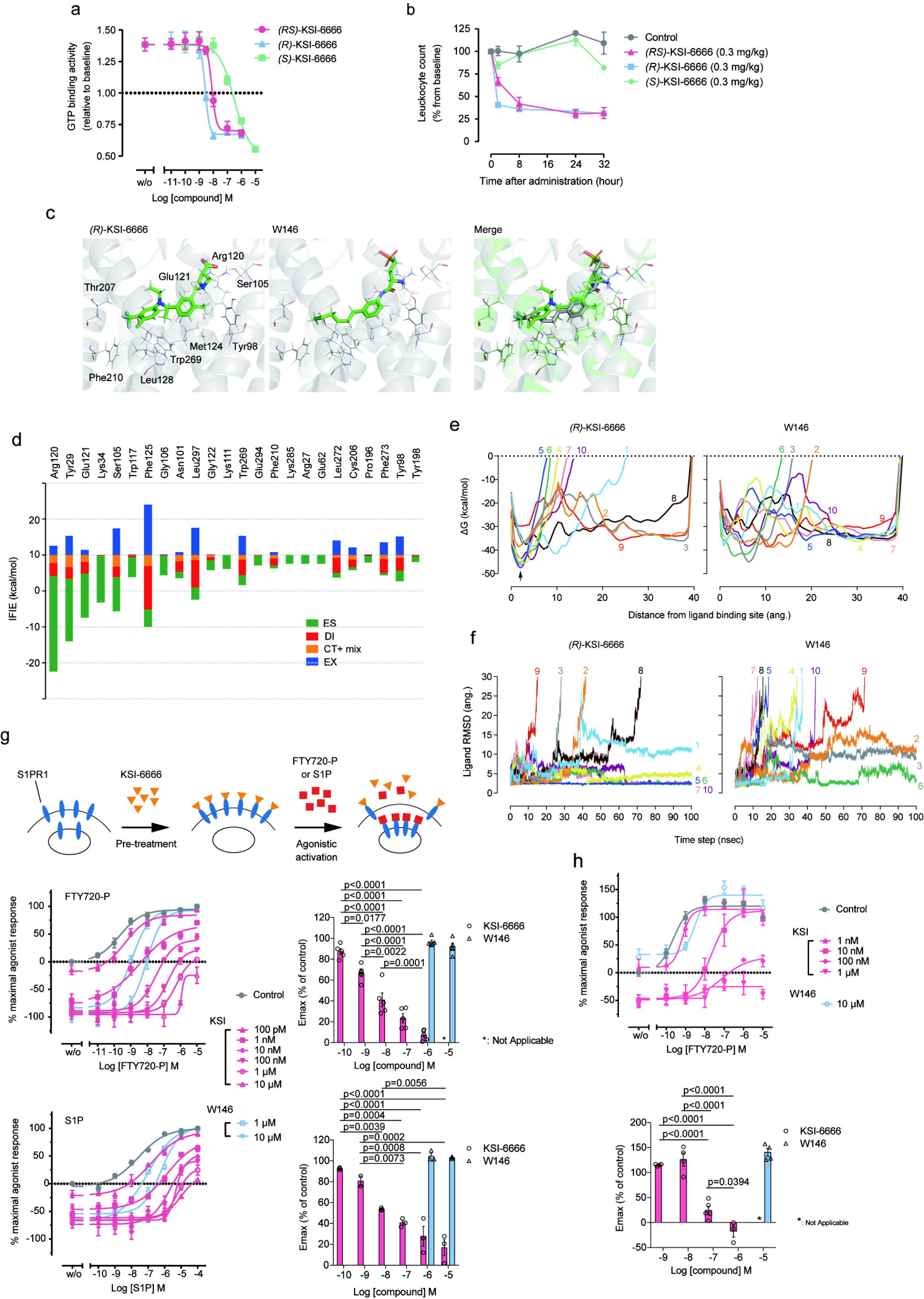
a
GTP binding activity (relative to baseline)
(RS)-KSI-6666
(R)-KSI-6666
(S)-KSI-6666
Log [compound] M
b
Leukocyte count (% from baseline)
Control
(RS)-KSI-6666 (0.3 mg/kg)
(R)-KSI-6666 (0.3 mg/kg)
(S)-KSI-6666 (0.3 mg/kg)
Time after administration (hour)
c
(R)-KSI-6666
W146
Merge
Arg120
Glu121
Ser105
Thr207
Met124
Tyr98
Trp269
Phe210
Leu128
d
IFIE (kcal/mol)
ES
DI
CT+ mix
EX
e
(R)-KSI-6666
W146
ΔG (kcal/mol)
Distance from ligand binding site (ang.)
f
(R)-KSI-6666
W146
Ligand RMSD (ang.)
Time step (nsec)
g
S1PR1
KSI-6666
Pre-treatment
FTY720-P or S1P
Agonistic activation
FTY720-P
% maximal agonist response
Control
KSI
100 pM
1 nM
10 nM
100 nM
1 μM
10 μM
Log [FTY720-P] M
Emax (% of control)
KSI-6666
W146
*: Not Applicable
S1P
W146
1 μM
10 μM
Log [S1P] M
Log [compound] M
h
% maximal agonist response
Control
KSI
1 nM
10 nM
100 nM
1 μM
W146
10 μM
Log [FTY720-P] M
Emax (% of control)
KSI-6666
W146
*: Not Applicable
Log [compound] M

Figure 4

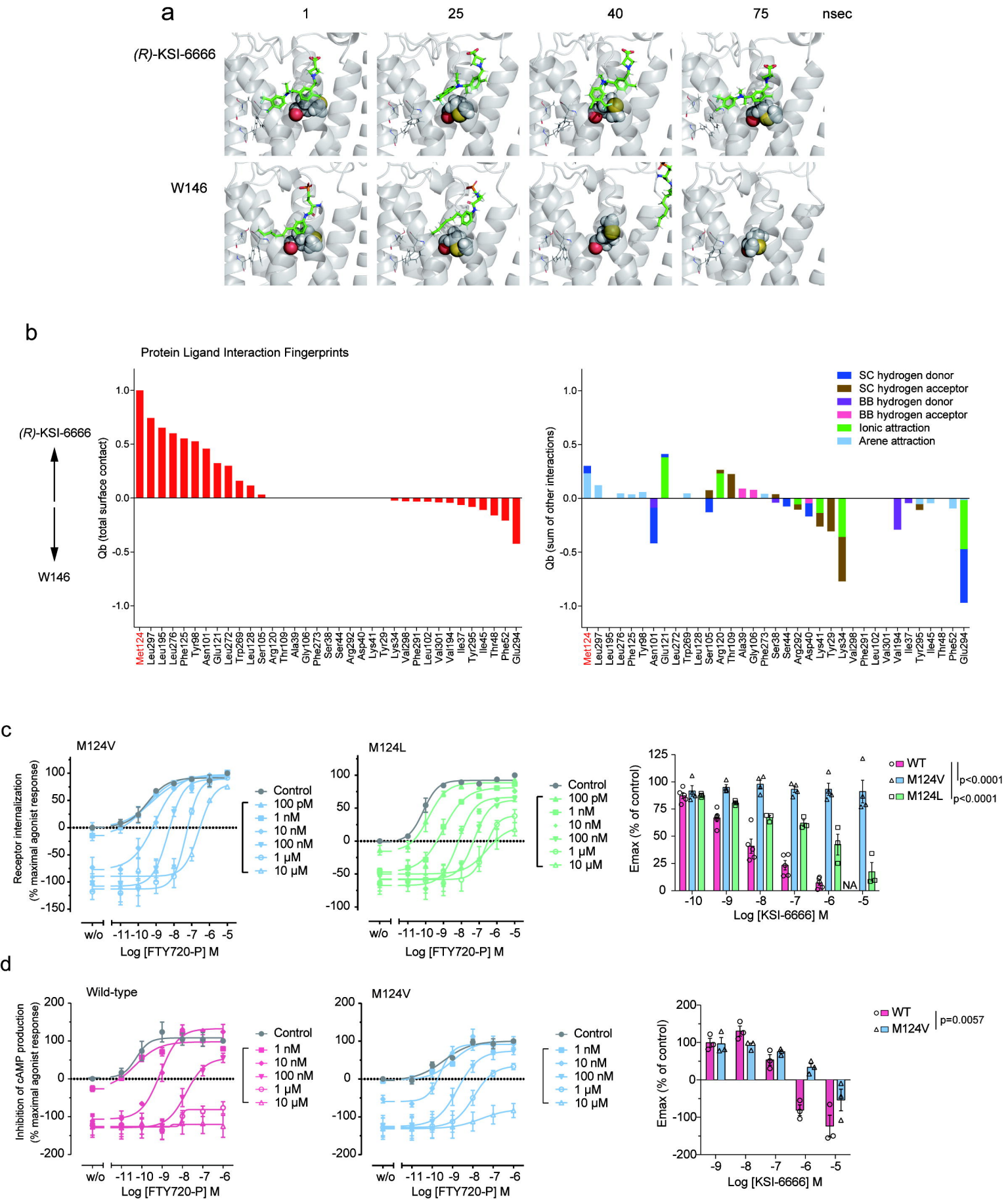
a
1
25
40
75
nsec
(R)-KSI-6666
W146
b
Protein Ligand Interaction Fingerprints
(R)-KSI-6666
W146
Qb (total surface contact)
Qb (sum of other interactions)
SC hydrogen donor
SC hydrogen acceptor
BB hydrogen donor
BB hydrogen acceptor
Ionic attraction
Arene attraction
Met124 Leu297 Leu195 Leu276 Phe125 Tyr98 Asn101 Glu121 Leu272 Trp269 Leu128 Ser105 Arg120 Thr109 Ala39 Gly106 Phe273 Ser38 Ser44 Arg292 Asp40 Lys41 Tyr29 Lys34 Val298 Phe291 Leu102 Val301 Val194 Ile37 Tyr295 Ile45 Thr48 Phe52 Glu294
c
M124V
M124L
Receptor internalization (% maximal agonist response)
Control
100 pM
1 nM
10 nM
100 nM
1 μM
10 μM
w/o
Log [FTY720-P] M
Emax (% of control)
WT
M124V
M124L
p<0.0001
p<0.0001
NA
Log [KSI-6666] M
d
Wild-type
M124V
Inhibition of cAMP production (% maximal agonist response)
Control
1 nM
10 nM
100 nM
1 μM
10 μM
w/o
Log [FTY720-P] M
Emax (% of control)
WT
M124V
p=0.0057
Log [KSI-6666] M

Figure 5

a

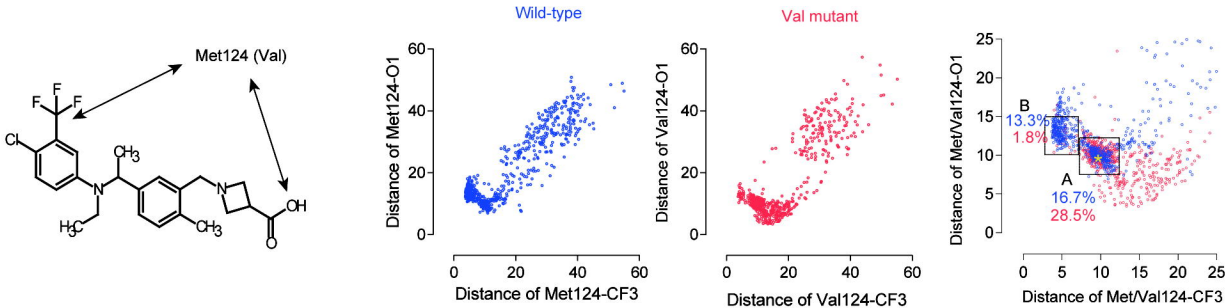
Met124 (Val)
Wild-type
Val mutant
Distance of Met124-O1
Distance of Met124-CF3
Distance of Val124-O1
Distance of Val124-CF3
Distance of Met/Val124-O1
Distance of Met/Val124-CF3
B
13.3%
1.8%
A
16.7%
28.5%

b

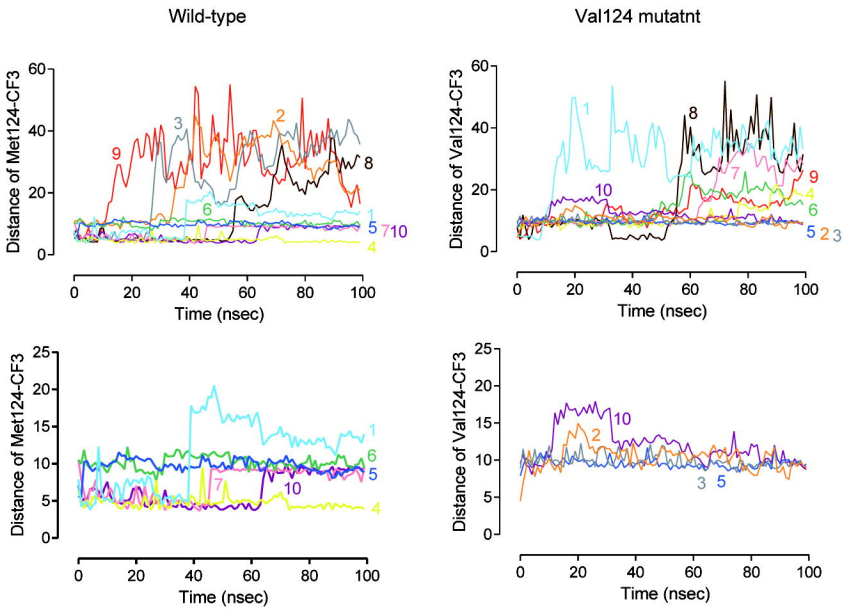
Wild-type
Val124 mutatnt
Distance of Met124-CF3
Distance of Val124-CF3
Time (nsec)

Figure 6

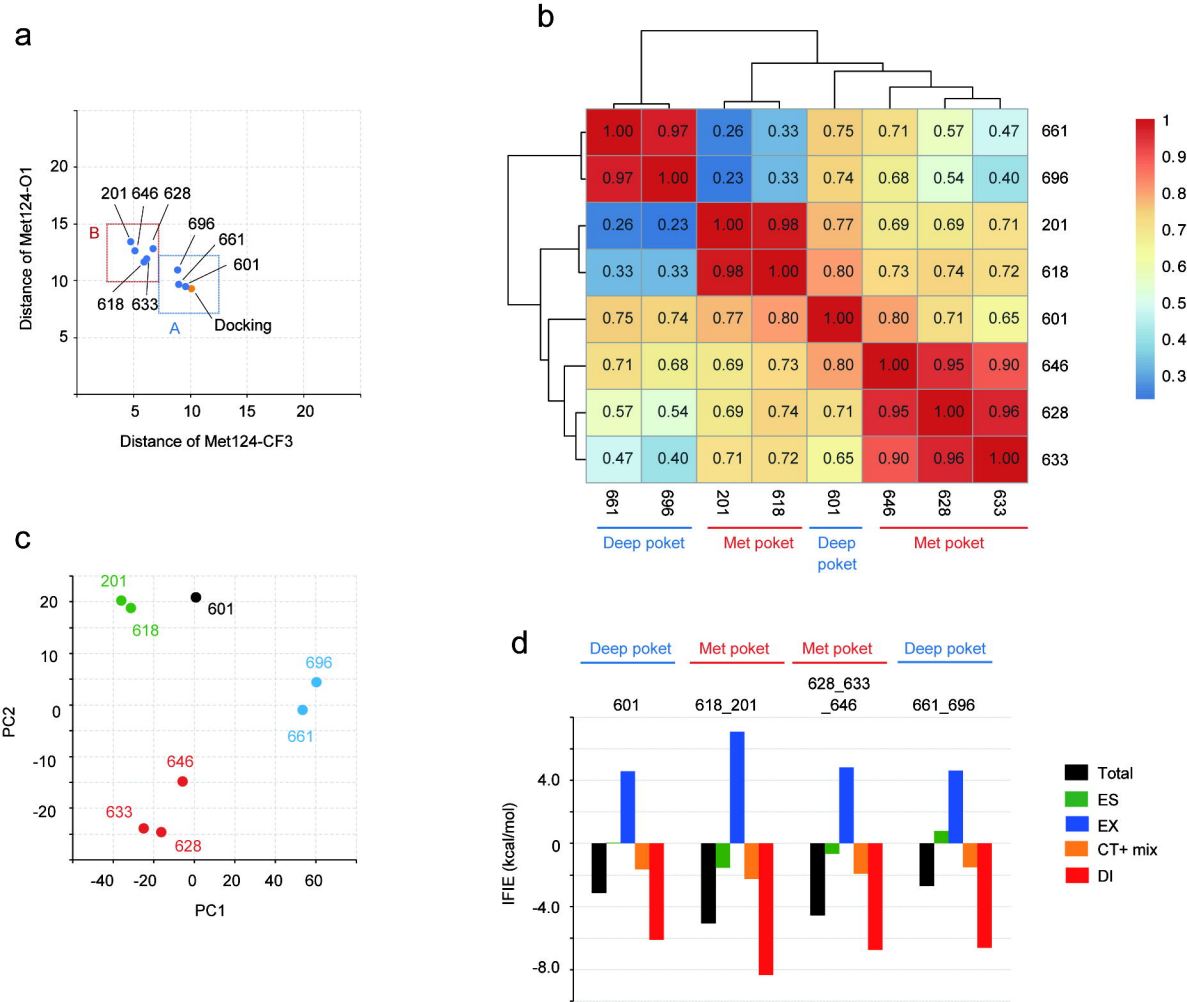
a
Distance of Met124-O1
Distance of Met124-CF3
201 646 628
696
661
601
618 633
Docking
A
B
b
661 696 201 618 601 646 628 633
Deep poket
Met poket
Deep poket
Met poket
c
PC1
PC2
201
618
601
696
661
646
633
628
d
Deep poket
Met poket
Met poket
Deep poket
601
618_201
628_633 _646
661_696
IFIE (kcal/mol)
Total
ES
EX
CT+ mix
DI

Figure 7

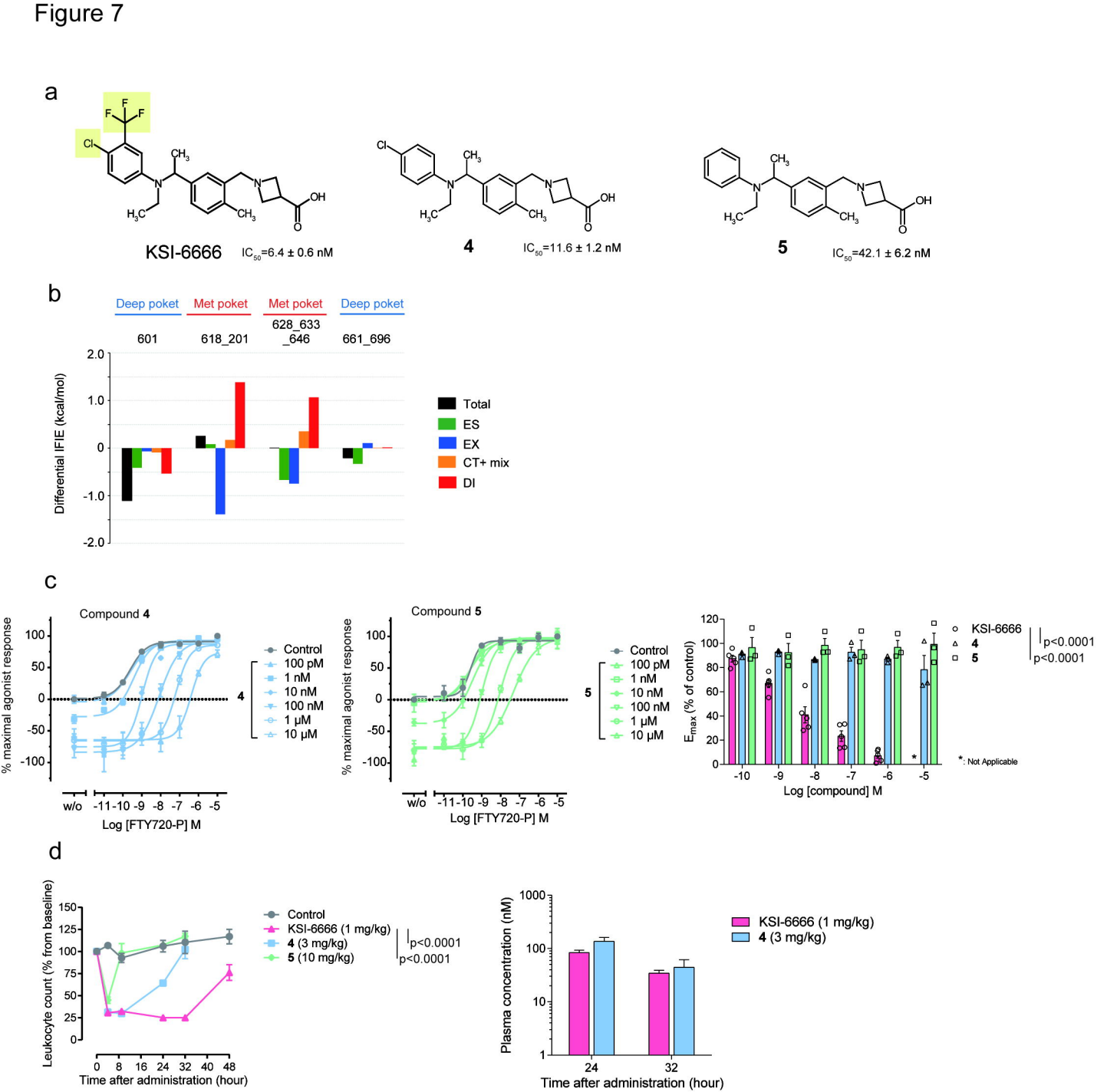
a
KSI-6666
IC50=6.4 ± 0.6 nM
4
IC50=11.6 ± 1.2 nM
5
IC50=42.1 ± 6.2 nM
b
Deep poket
Met poket
Met poket
Deep poket
601
618_201
628_633
_646
661_696
Differential IFIE (kcal/mol)
Total
ES
EX
CT+ mix
DI
c
Compound 4
Compound 5
% maximal agonist response
Log [FTY720-P] M
Control
100 pM
1 nM
10 nM
100 nM
1 μM
10 μM
Emax (% of control)
Log [compound] M
KSI-6666
p<0.0001
p<0.0001
*: Not Applicable
d
Leukocyte count (% from baseline)
Time after administration (hour)
Control
KSI-6666 (1 mg/kg)
4 (3 mg/kg)
5 (10 mg/kg)
p<0.0001
p<0.0001
Plasma concentration (nM)
KSI-6666 (1 mg/kg)
4 (3 mg/kg)